MICHIGAN STATE UNIVERSITY

CYCLOTRON LABORATORY

LIGHT PARTCLE-COMPLEX FRAGMENT COINCIDENCE CROSS SECTIONS FROM INTERMEDIATE ENERGY NUCLEUS-NUCLEUS COLLISIONS

B.E. HASSELQUIST, G.M. CRAWLEY, B.V. JACAK, Z.M. KOENIG, G.D. WESTFALL, J.E. YURKON, R.S. TICKLE, J.P. DUFOUR and T.J.M. SYMONS

MAY 1985

MSUCL-519

MSUCL-519
May 1985

Light Particle-Complex Fragment Coincidence Cross Sections from Intermediate Energy Nucleus-Nucleus Collisions

B.E. Hasselquist*, G.M. Crawley, B.V. Jacak†, Z.M. Koenig, G.D. Westfall and J.E. Yurkon

National Superconducting Cyclotron Laboratory
Michigan State University
East Lansing, Michigan 48824-1321

R.S. Tickle

Department of Physics, University of Michigan
Ann Arbor, Michigan 48109-1120

J.P. Dufour** and T.J.M. Symons

Lawrence Berkeley Laboratory
University of California, Berkeley, California 94720

Light particle ($Z \leq 2$) inclusive and coincidence spectra have been measured for the reactions 30 MeV/nucleon ^{12}C+Al and ^{12}C+Au and 92 MeV/nucleon ^{40}Ar+Au at angles from 45 to 90°. Coincidence triggers for the light particle spectra were intermediate rapidity fragments ($3 \leq Z \leq 7$) at -30° and projectile-like fragments ($3 \leq Z \leq 18$) at -13°. The Ar+Au inclusive spectra are compared to hydrodynamics and firestreak model calculations. Non-azimuthally averaged hydrodynamics calculations are compared to the light particle spectra triggered by projectile-like fragments. A single moving source parameterization is employed throughout to extract the relevant trends in the inclusive and coincidence data. The coincidence spectra are compared with a model based on the moving source model but incorporating momentum conservation to account for kinematical biasses. Little difference between inclusive and complex-fragment-triggered coincidence cross sections is observed indicating that all the fragments have a common source.

I. Introduction

In the past decade experimental efforts in the field of heavy ion nuclear physics have concentrated on projectile energy regions below 20 MeV/nucleon and above 200 MeV/nucleon. The energy range in between is a particularly interesting regime because it covers projectile velocities ranging from below the fermi velocty in nuclei up to velocities several times the speed of sound in nuclei. New accelerators operating in this energy range have led to a number of investigations of inclusive light particle production from carbon-, oxygen-, neon-, and argon-induced reactions.[1-11] The double differential cross sections for particles with $1 \leq A \leq 4$ indicate the existence of a thermalized emission source moving at a velocity intermediate between the target and projectile velocities.[3,5,7] Fragment production cross sections for 42, 92, and 137 MeV/nucleon ^{40}Ar-induced reactions suggest that all intermediate rapidity particles ($1 \leq A \leq 14$) originate from a common source.[5] It is clear however that light particles and complex fragments may originate from different impact parameter collisions.[12] Results from 4π detectors such as the Plastic Ball[13] demonstrate that inclusive measurements are not sufficient to delineate clearly between various models for the reaction mechanisms.

To clarify the source of high energy fragments from these collisions we have measured the production of light particles in coincidence with projectile-like fragments (PLFs) which originate in gentle, grazing collisions and with intermediate rapidity fragments (IRFs) which come from highly inelastic collisions. By studying the properties of the light particle spectra triggered by these different classes of events and by comparing to the untriggered, inclusive data one may examine the differences between peripheral and more central collisions yielding complex fragments.

In reactions at 30 MeV/nucleon one has just enough energy to completely unbind all the nucleons in both the projectile and target in a completely inelastic collision. At 92 MeV/nucleon there is much more energy than necessary to unbind the nucleons and one might expect such phenomena as hydrodynamic behavior to become important. In fact the study of hydrodynamics might be especially fruitful at this rather low energy as compared to energies such as 2 GeV/nucleon because of the much decreased thermal background.

The present work investigates the dependence of the light particle spectra ($Z \leq 2$) on fragment production for the reactions ^{12}C + Al and Au at 30 MeV/nucleon and ^{40}Ar + Au at 92 MeV/nucleon. Light particle spectra for complex fragment triggers with $3 \leq Z \leq 6$ were obtained for the ^{12}C-induced reactions and spectra for trigger fragments with $3 \leq Z \leq 18$ were obtained for the ^{40}Ar-induced reaction. The complex fragments were either PLFs or IRFs depending on the angle of the trigger counter (forward angles are projectile-like and wider angles come from more violent reactions) and the energy ranges of the particle detectors.

In order to quantify the changes in the triggered light particle spectra, we have parametrized the spectra with a moving source model where the temperature, cross section and source velocity are extracted. These parameters are compared for inclusive and triggered data. Hydrodynamics[14] and firestreak[15] calculations have been compared with the ^{40}Ar-induced inclusive spectra. A hydrodynamics calculation has also been performed for the ^{40}Ar-induced coincidence spectra. To illustrate possible contributions from simple kinematics and conservation laws in the coincidence spectra, we also present a momentum conservation model calculation.

II. Experimental Setup

The 30 MeV/nucleon measurements were carried out using the K500 superconducting cyclotron at the National Superconducting Cyclotron Laboratory. The ^{12}C beam intensities varied from 0.33 particle namps ($2X10^9$ particles/sec.) to 2.5 particle namps ($1.5X10^{10}$ particles/sec) and were monitored with a faraday cup and current integrator. The resulting normalizations were good to 20%. The targets consisted of 3.0 mg/cm^2 Al and 2.0 mg/cm^2 Au. The 92 MeV/nucleon work was done with the Bevalac at the Lawrence Berkeley Laboratory where the ^{40}Ar beam intensity averaged 10^7 particles/pulse with a beam pulse occurring every 4 sec. The intensity was measured using an ion chamber calibrated with a plastic scintillator that counted the beam particles at low intensity. The absolute cross sections were known to 10%. The target was 213 mg/cm^2 Au.

The experimental apparatus consisted of an array of light particle detectors on one side of the beam axis along with two sets of complex fragment detectors placed on the opposite side of the beam. One set of fragment detectors was placed at forward angles and the dynamic range of the counters was set to detect PLFs ranging from the beam down to Li. These fragments generally had energies corresponding to the projectile energy/nucleon. The second set of triggers was designed to detect IRFs and was placed at angles outside the region of PLFs with the dynamic range of the counters set to detect Li-O fragments. The arrangement and composition of the detectors for all cases is given in Table 1 and representative dynamic ranges are given in Table 2.

The light particle telescopes in the array were capable of determining the energy and identity of light nuclei (p,d,t,^{3}He and ^{4}He). The energy ranges of detected particles are given in Table 2. The array consisted of

seven NE102 plastic scintillator-CaF_2 "phoswich" telescopes each of which used a single photomultiplier tube to collect both the plastic scintillator and the CaF_2 signal. The two signals were distinguished by means of their different decay times. The decay time for the plastic scintillator was less than 10 nsec compared to 1 μsec for the CaF_2. Integration of the photomultiplier output in a charge integrating ADC for the first 80 nsec gave most of the plastic scintillator signal. A separate integration in another charge integrating ADC over a period of 2 μsec delayed by 240 nsec relative to the beginning of the first integration gave the CaF_2 signal. The plastic scintillator was 17 cm thick and functioned as the stopping E detector. The CaF_2 was 2mm thick and functioned as the energy loss ΔE detector. The telescope array was moved during the experiments and covered in-plane angles from approximately 38 to 97°.

The energy calibration of the telescopes was done using ^{4}He beams of 25 MeV/nucleon at NSCL and 150 MeV/nucleon p and ^{4}He at LBL. The light particle inclusive and coincidence spectra have been corrected for reaction losses in the scintillators and for particles scattering out of the detectors.

The fragment detectors were composed of stacks of silicon detectors. The thicknesses are listed in Table 1. Two different IRF stacks were used in the 92 MeV/nucleon work to provide sufficient dynamic range. The first silicon detector determined the low energy cutoff and was chosen to exclude target-like fragments. Representative dynamic ranges are listed in Table 2. The PLF detectors were placed outside the grazing angle to suppress elastic scattering. The grazing angles for 30 MeV/nucleon ^{12}C+Al, ^{12}C+Au, and 92 MeV/nucleon ^{40}Ar+Au were 3°, 12°, and 3° respectively.

III. Results and Discussion

Energy spectra from all of the telescopes in the scintillator array at a given angle setting have been summed together to obtain the best possible statistics and the errors depicted in the energy spectra are statistical. Positive detector angles imply the side of the reaction plane on which the scintillator array was placed while negative angles imply the opposite side.

III A. Inclusive Light Particle Spectra

Light particle inclusive spectra have been measured for the reaction 30 MeV/nucleon ^{12}C+Al at the angles 45, 56, 71, and 90° and at 45,49,56, 71 and 90° for 30 MeV/nucleon ^{12}C+Au. The 45 and 49° spectra for the Au target have been combined because of low statistics at the 45° setting. An average angle of 47° will be used for the combined spectra. Energy spectra for the hydrogen isotopes are shown in Fig. 1. The solid curves in the figure are moving source fits to the data as described below. The spectra are smooth and change monotonically with angle. The low energy cutoff of the telescopes minimizes the contribution of target-like particles and there is a slight indication of projectile-like spectra in the 45° spectra. The contributions from projectile evaporation can be more clearly seen in the d and t spectra shown in Fig. 2. These inclusive spectra were measured in a separate experiment for the reaction 30 MeV/nucleon ^{12}C+Au at angles of 15, 45, 75, 90 and 105° in the laboratory. The peaks in the 15° cross sections at energies of approximately 30 MeV/nucleon are evidence of projectile evaporation. It can be seen that there is still a contribution from projectile evaporation at 45°.

Light particle inclusive spectra have been measured for the reaction 92 MeV/nucleon ^{40}Ar+Au at angles of 45, 67.5, and 90° in the laboratory. Energy spectra for p, d, t, ^{3}He and ^{4}He are shown in Fig. 3. As in the lower energy case, the energy spectra are featureless and vary smoothly with angle. No

contribution from projectile-like or target-like particles is evident. Again the solid lines correspond to moving source calculations. The 92 MeV/nucleon inclusive data are qualitatively similar to the 30 MeV/nucleon data. There is no drastic change in the inclusive light particle spectra in spite of the differences in the incident energies.

III B. Moving Source Model

We fit the light particle spectra with a single moving source parameterization. By fitting the spectra and extracting parameters describing the source of the observed particles one can quantitatively compare light particle spectra from different systems and trigger conditions. This method has been applied to inclusive light particle and complex fragment spectra for a variety of systems.[3,5,7] In this model a source emits particles isotropically in its rest frame which moves at a fraction of the beam velocity. The energy spectra are assumed to be a relativistic Maxwell-Boltzmann energy distribution in the source rest frame given by[16]

$$\frac{d^2\sigma}{p^2 dp d\Omega} = \frac{\sigma}{4\pi m^3} \frac{\exp(-E/\tau)}{2(\tau/m)^2 K_1(m/\tau)+(\tau/m)K_0(m/\tau)} \qquad (1)$$

where p and E are the momentum and total energy, respectively, of a particle in the source rest frame, and K_0 and K_1 are modified Bessel functions of the second kind. The spectra are fit using the method of least squares. The three fit parameters are σ, the production cross section, β, the velocity of the moving source, and τ, the slope parameter, which is referred to as the temperature of the source. The moving source calculations are shifted up in energy to account for the coulomb barrier of the emitting system. The coulomb shifts used in the analysis of the Au target data at both energies were 10 and 18 MeV for Z=1 and 2, respectively. For the Al target data, shifts of 4 and 8

MeV were used for Z=1 and 2, respectively. For the 30 MeV/nucleon data, the lower energy cuts for the fits were 30, 20, and 20 MeV/nucleon for p, d, and t, respectively to eliminate contributions from target evaporation. The most forward angle data were not included in the fits in order to eliminate contributions from projectile evaporation. The 92 MeV/nucleon fits included all the angles and energies above 50 MeV/nucleon. The same cuts and shifts will be used for the coincidence spectra.

The extracted moving source parameters for inclusive data are given in Table 3. At 30 MeV/nucleon the extracted source temperatures for the two targets are quite similar. The source velocities for the Al target spectra are ≈30 percent higher than for the Au target. The fireball model and the systematics of the moving source parameterization predict that the source velocity should scale as the velocity of the center of mass of the colliding system. For C+Al and C+Au, the ratio of the center of mass velocities is about 1.35 in agreement with the observed velocities. The temperatures and velocities agree with systematics of O- and Ne- induced reactions on heavy targets[3] as shown in Fig. 4. However the production cross sections differ systematically from these results. To illustrate this deviation the proton production cross sections from O- and Ne-induced reactions are shown in Fig. 5 along with the present results. The solid line is a smooth line drawn through the O- and Ne- induced data.[3] The dashed and dot-dashed line correspond to a scaling of this smooth behavior for C- and Ar-induced reactions using an expression for the scaling of proton total cross section,[17]

$$\sigma_{tot} \propto Z_p(A_t^{2/3})+Z_t(A_p^{2/3}). \qquad (2)$$

The scaled lines agree roughly with the present data and with other C-[7] and Ar-induced[5] results.

III C. Hydrodynamics and Firestreak Models

In Fig. 6 inclusive light particle spectra from 92 MeV/nucleon ^{40}Ar+Au are compared with a relativistic hydrodynamics (HD) calculation and with a firestreak (FS) model calculation. The solid curves in the figure correspond to HD calculations by Buchwald.[14] These calculations predict the spectra of light nuclei rather than just nucleons by incorporating thermal and chemical equilibrium in the nuclear matter emitted during the collision. The results are presented with arbitrary normalizations for each particle: p X10; d X3.3; t X0.13; ^{3}He X1; and ^{4}He X0.33. These discrepancies are attributed to the simplicity of the thermal model used to predict the spectra of the light nuclei. The HD results are azimuth and impact parameter averaged for impact parameters from 0 to 7 fm. The dot-dashed curves are firestreak (FS) calculations for the same system.[15] Neither calculation fits the proton spectra well while both fit the deuteron spectra. The HD calculation tends to give a more realistic fit to the other spectra. This difference is most obvious at the low energy end of the spectra where the FS calculation tends to overpredict the cross sections.

Although the agreement of these two models with the data is not quantitative, the results of both calculations taken together imply that thermal concepts have an important role in the description of these collisions. The models describe the qualitative behavior of the angular distributions, overall normalizations (with the above exceptions for HD), and slopes of the energy spectra. Some of the apparent disagreement arises because the models explicitly do not treat the spectator nuclei which can contribute to the observed spectra.

IV A. IRF Triggered Light Particle Spectra

To focus on more central collisions, we have measured light particles in coincidence with high energy complex fragments emitted at wide angles. These trigger fragments are not associated with either the projectile or target nuclei but instead appear to be emitted from a source moving with velocity or rapidity intermediate between the projectile and target velocities. Because emission of such fragments requires the formation of a large intermediate rapidity source, these fragments cannot originate from the gentle, peripheral collisions that contribute strongly to inclusive spectra and one expects qualitative differences between light particle spectra triggered on such fragments and inclusive spectra. All of the coincidence spectra presented below have been divided by the solid angle of the trigger detector. The limits imposed on the integration of the trigger particle spectra are those imposed by the lower and upper energy cutoffs of the detector, except where noted.

The inclusive fragment spectra ($3 \leq Z \leq 6$) for the IRF trigger at $-25°$ are shown in Fig. 7 for 30 MeV/nucleon ^{12}C incident on Al and Au targets. The shapes of the spectra are quite similar for all the IRFs and indicate these fragments are created by similar mechanisms. Proton and deuteron spectra triggered on IRFs with $3 \leq Z \leq 6$ for 30 MeV/nucleon ^{12}C+Al are shown in Figs. 8 and 9, respectively. Light particle spectra for coincidences between protons and deuterons and IRFs ($3 \leq Z \leq 6$) from 30 MeV/nucleon ^{12}C+Au are shown in Fig. 10. In this case the spectra for all trigger fragments have been summed together to obtain satisfactory statistics.

The inclusive fragment spectra ($3 \leq Z \leq 7$) for the IRFs from 92 MeV/nucleon ^{40}Ar+Au are shown in Fig. 11. The data have been plotted as invariant cross sections as a function of the total fragment momentum. The solid lines in this figure are to guide the eye. The similarity of the shapes of the cross

sections is an indication that a single reaction mechanism is responsible for the production of the various fragments. This phenomenon has been examined in detail in Ref. 5 where it was shown that the inclusive fragment spectra from 30 to 90° in the laboratory frame could be explained with the assumption of fragment emission from a single intermediate rapidity thermal source.

Spectra for p, d, t, ^{3}He and ^{4}He coincident with IRFs from 92 MeV/nucleon ^{40}Ar+Au are shown in Figs. 12-16. The inclusive light particle spectra have been included in the figures for comparison with the coincidence spectra. The coincidence spectra have the same general features as the inclusive spectra for all measured light particle - IRF combinations suggesting that these fragments have a common source.

The solid curves in the Figs. 8-10 and Figs. 12-16 are moving source fits to the IRF-triggered data and the extracted parameters are given in Table 4. The energy and angle cuts for these fits are the same as those used in the inclusive results presented above. The moving source fits for the 30 and 92 MeV/nucleon data triggered on IRFs describe the data very well and only deviate significantly for p-Li coincidences from both targets at 30 MeV/nucleon.

The extracted temperatures and velocties for the IRF triggered light particle coincidence spectra tabulated in Table 4 are shown in Figs. 17 and 18 as ratios of the coincidence values divided by the inclusive values. The results for 30 MeV/nucleon ^{12}C+Au are not shown in these figures because they are summed over the trigger fragment mass. The ratios given in Figs. 17a and 18a demonstrate that the extracted IRF-triggered temperatures tend to be about 5% higher than the inclusive temperatures at 92 MeV/nucleon but are about the same at 30 MeV/nucleon. There does not appear to be any statistically significant variation in this parameter over the range of trigger fragments

measured and Figs. 17c and 18c show that the extracted coincidence spectra velocities tend to be lower than the inclusive velocities by about 10%. There are indications of a decrease in the velocity parameter with increased trigger fragment mass. There seems to be no significant dependence of the temperature and velocity parameters on the particular type of light particle measured. The apparent differences between the ^{3}He parameters and those of the other light isotopes may be due to the lower statistics of the ^{3}He spectra.

The slightly lower apparent velocities for the coincidence spectra relative to the inclusive spectra may be due to the inclusion of the 45° data in all of the moving source fits. The size of the scintillator array gave an angular acceptance at the 45° setting forward to ≈ 35° and may include contributions from projectile evaporation at energies corresponding to the beam velocity. However, it is likely that detection of intermediate mass fragments at -30° selects events in which the projectile either disintegrates or is appreciably slowed so that the IRF triggered light particle spectra would not have contributions from projectile evaporation that might be included in the inclusive data.

IV B. PLF Triggered Light Particle Spectra

It is possible to observe evidence of three distinct reaction mechanisms in the PLF fragment spectra; projectile fragmentation, thermal emission, and few nucleon transfer. Projectile fragmentation has been described as an interaction occurring for large impact parameters in which the incoming projectile nucleus becomes excited upon contact with the target nucleus. The projectile velocity is not appreciably reduced by the collision as it would be for a collision at a smaller impact parameter. The excited projectile either breaks up near the target nucleus before equilibration of the excitation energy or decays in flight after thermal equilibrium is established. The

momentum distribution for a fragment emitted from a decaying projectile has been described by Goldhaber[18] using a gaussian distribution. For a fragment with K nucleons emitted from a projectile with A nucleons the momentum width is given as

$$\sigma_p^2 = \sigma_{p_o}^2 K(A-K)/(A-1), \qquad (3)$$

where $\sigma_{p_o} \approx 100$ MeV/c. The value of σ_{p_o} can be related to the fermi momentum of the nucleons, p_f, in the projectile nucleus by $\sigma_{p_o} = p_f/\sqrt{5}$. Projectile fragmentation has been observed in Ar-induced reactions on C and Th at 213 MeV/nucleon[19] as well as at energies below 100 MeV/nucleon in ^{12}C- and ^{40}Ar-induced reactions.[9-11] An exponential fall-off of the energy spectra is consistent with the assumption of emission from a thermal source. The few nucleon transfer reaction mechanism involves the exchange between the target and projectile nuclei of one or several nucleons. The fragment velocity distributions for the transfer process are characterized by narrow peaks centered at the beam velocity. The narrow peak widths can be attributed to the limited range of energies of the available excited states into which the exchanged nucleons can be transferred.

The inclusive fragment spectra ($3 \leqq Z \leqq 6$) for the PLF trigger are shown in Figs. 19a and 19b for 30 MeV/nucleon ^{12}C + Al and Au , respectively. The spectra have been plotted as a function of the ratio of the detected fragment velocity over the incident projectile velocity. One clearly sees a peak near the projectile velocity for B and C PLFs but Li and Be fragments show an exponential spectrum rather than one peaked at the beam velocity.

Coincidence spectra between protons and projectile velocity fragments from 30 MeV/nucleon ^{12}C + Al are shown in Fig. 20. The PLF triggered proton

and deuteron spectra for 30 MeV/nucleon ^{12}C + Au are shown in Fig. 10 where the spectra are summed over all the PLFs to improve the statisitics. For both targets, the 45 and 56° spectra are nearly identical in both shape and magnitude. A comparison of the PLF triggered spectra with the IRF triggered proton spectra in Fig. 10 suggests that the 56° spectra are anomalously high compared to the rest of the angular distribution.

The inclusive double differential cross sections for the projectile-like fragment (PLF) trigger at -13° are shown in Fig. 21 for 92 MeV/nucleon ^{40}Ar + Au. Cross sections are shown for fragments with ($3 \leq Z \leq 18$) as a function of the ratio of the fragment velocity to the incident projectile velocity. The velocity distributions which most clearly show projectile fragmentation are those for O through P fragments. The observed peaks appear guassian in shape with centroids between 85 and 90% of the projectile velocity that can, in part, be accounted for by the loss in kinetic energy of the emitting system due to the binding energy associated with the emitted fragment. The Li and Be fragment velocity distributions are primarily exponential in shape with only slight shoulders to indicate the possible presence of projectile fragmentation phenomena. The B, C, and N velocity distributions show evidence of both fragmentation and thermal emission.

The B and C spectra in Fig. 19 and the S, Cl and Ar fragment velocity distributions in Fig. 21 appear to be dominated by the few nucleon transfer mechanism as shown be the markedly narrower widths and higher velocities relative to those of the lighter mass fragments. The apparent sudden change from fragmentation to transfer reactions at sulfur in ^{40}Ar fragmentation has been examined more closely in Refs. 9 and 12 in reactions at 44 and 27.6 MeV/nucleon, respectively. In this work the mechanism changes from fragmentation to few nucleon transfer between ^{35}S and ^{36}S. Formation of a fragment

smaller than ^{36}S from ^{40}Ar would require the transfer to the target of a fragment larger than an alpha particle.

Light particle spectra for coincidences between p, d and t and projectile-like fragments are shown in Figs. 22-24. The spectra for coincident fragments with $9 \leq Z \leq 15$ have been summed together to obtain reasonable statistics. The inclusive light particle spectra have been included in these figures for comparison with the coincidence spectra. The light particle coincidence spectra for the Li through N PLF triggers appear to be very similar to the inclusive spectra. It can be seen from Fig. 22 that the proton coincidence cross sections for the O and the F through P PLF triggers have a slightly flatter angular distribution than the inclusive cross sections characteristic of a lower source velocity. A similar trend is seen for the deuteron spectra while the statistics are insufficient to observe this difference for coincident tritons.

The three reaction mechanisms discussed above need to be taken into account when attempting to understand the light particle coincidence data. For coincidences with fragments with $Z \leq 7$, the contributions from thermal sources are non-negligible. A picture which includes fragmentation and thermal emission is necessary. For coincidences with fragments with $8 \leq Z \leq 15$, fragmentation along with few nucleon transfer must be considered although there will undoubtedly still be contributions to the light particle spectra from emission from a moving thermal source as well as target evaporation. Coincidence events with the highest three Z fragments might be expected to yield light particles originating primarily from target evaporation. The inclusive PLF spectra for fragments with $Z \leq 7$ exhibit substantial contributions from thermal source emission associated with central collisions. It is therefore not surprising that the light particle coincidence spectra associated with these fragments are

similar to the inclusive spectra and the IRF triggered spectra. For fragments at -13° with $8 \leq Z \leq 15$, the inclusive PLF spectra are dominated by projectile fragmentation that must necessarily be peripheral and therefore, less likely to create an excited moving source. There are two likely primary sources of emission for this type of collision; emission from the fragmenting projectile which would be focussed in the direction of the projectile and emission from the excited target which would be isotropic in the laboratory frame. The light particle spectra measured in this experiment are well away from the measured fragment direction. The observation of lower apparent source velocities for the proton and deuteron spectra is therefore consistent with emission from the excited target. There is still a contribution from an intermediate source although it appears to be diminished.

Light particle - fragment coincidence spectra for fragments with $Z \geq 16$ had insufficient statistics to study the reaction mechanisms involved. If the mechanism for these fragments is few nucleon transfer, one would expect that the associated light particle coincidence rate is low. The low number of observed coincidence events is consistent with this expectation.

The extracted moving source fit parameters are given in Table 5. The temperatures and velocities are plotted in Figs. 17 and 18 as ratios of the coincident values to the inclusive values. Note that the parameters for spectra summed over coincidences with F through P fragments are plotted at an approximate average mass of 24. As was true for the light particle - IRF spectra, the temperature parameter shows no variation with the PLF trigger fragment mass. In addition, the PLF triggered spectra source temperatures are the same as the inclusive temperature. This constancy could reflect the fact that the PLF spectra at 13° may contain a large contribution from thermal sources. In contrast, the velocities show a clear trend toward decreasing

velocities with increasing trigger fragment mass for the proton and deutron spectra. An apparent velocity 30 percent below the inclusive result is obtained for the average projectile mass of A=24 which is consistent with the concept of emission from an excited residual target nucleus. The triton spectra velocities do not decrease with trigger coincident fragment mass and in fact, are very nearly constant. One might speculate that triton spectra which are observed between 45 and 90° are dominated by the contributions from more central collisions or alternatively by emission from whatever intermediate source might be created in the process leading to projectile fragmentation.

IV C. Momentum Conservation Model

The interpretation of coincidence spectra has as an inherent hazard the possibility of assigning special significance to phenomena which had their origins in simple conservation laws. The calculation presented here assumes that two coincident particles are emitted sequentially from a single moving source.

From a knowledge of the momentum of the first particle, it is possible to calculate the reduction in excitation energy of the source and its recoil momentum. The second particle is then emitted from the cooled, recoiling source. Since it is not possible to know which particle was emitted first, both time sequences are combined to give the final coincidence cross section. The initial source parameters used in the calculations were moving source parameters extracted from the inclusive light particle spectra for the particle of interest. The size of the emitting source was chosen to correspond to the size of the fireball (FB) formed at the most probable impact parameter. This assumption gave source sizes of A=82 for the Ar+Au reaction and A=18 and 38 for the C+Al and C+Au reactions, respectively . The normalizations of the

final calculated coincidence cross sections were obtained using cross sections from moving source fits to the inclusive spectra of both emitted particles. The intermediate mass fragment cross sections for the Ar+Au reaction were obtained from Ref. 5. The spectra were further normalized by dividing by the reaction cross section. There were no other free parameters in the Ar+Au normalizations. Fragment cross sections were not available for the 30 MeV/nucleon reactions thus the calculated spectra for the 30 MeV/nucleon reactions were arbitrarily normalized in order to compare the shapes of the distributions. A more detailed description of the calculation is available in Ref. 20.

The results of the momentum conservation model for 30 MeV/nucleon induced coincidence spectra triggered by IRFs are shown as dot-dashed lines in Figs. 8-10 and 20. Based on the assumption that IRFs originate from a fireball-like system, this model should demonstrate the effect of simple momentum conservation on the coincidence spectra. For the case of ^{12}C + Al the model calculation with the FB geometry prediction of A=18 exhibited extreme effects due to the source recoil that were not observed in the data. To obtain better agreement with the data the source size was increased to A=27 and the results of these calculations are shown in Figs. 8, 9 and 20 as dot-dashed lines. This calculation is in fair agreement with the data, although, there is still a flatter slope for the proton spectra with heavier IRF trigger fragments and for the deuteron spectra. This comparison suggests that the emitting source is larger than A=27 and perhaps could be as large as the projectile/target system rather than a subset of the nucleons. For ^{12}C + Au the model reproduces the observed correlations but the statistics were poor. In contrast to the 30 MeV/nucleon data, the IRF triggered spectra at 92 MeV/nucleon are well described by this model using the FB geometry as shown in

Figs. 12-16 in the form of dotted lines. The only discrepancies appear at low energies and in some of the overall normalizations. This system apparently has sufficient kinetic energy and number of particles to make momentum conservation effects negligible.

For PLF-triggered spectra the model should only describe light particle spectra in coincidence with PLFs that exhibit a thermal rather than a projectile-like velocity distribution. Indeed the results of this calculation shown in Fig. 20 for 30 MeV/nucleon ^{12}C + Al as dot-dashed lines agree for Li PLFs and disagree for C PLFs. This result indicates that the C PLFs are fragmentation products and are not emitted from the same source as the light particles.

Fig. 25 shows the results of the hydrodynamics (HD) calculations of Buchwald[13] for the reaction 92 MeV/nucleon ^{40}Ar+Au compared to p and d spectra triggered by PLFs from F to P at -13°. The observation of the PLF determines the reaction plane. The dot-dashed lines are the predicted p and d spectra for θ=45, 70 and 90° and an azimuthal angle of ϕ=180°. An azimuthal angle of ϕ=180° corresponds to the opposite side of the reaction plane in which the projectile nucleus is scattered in the HD calculation. The calculation is averaged for impact parameters from 0 to 7 fermi. The calculation is not azimuthally averaged as was the HD calculation used in comparison to the inclusive light particle spectra. The normalizations are arbitrary to allow comparisons of the shapes. The hydrodynamics prediction for ϕ=0° can be characterized by the enhancement of the forward angle spectra while the ϕ=180° prediction is almost isotropic. Hydrodynamics predicts that for collisions which are not head-on, the incident projectile is inelastically scattered from the target nucleus into the ϕ=0° side of the reaction plane and then decays by

emission of light particles. The light particles are focussed in the direction of the scattered projectile due to its relatively high velocity. The target nucleus is also excited and decays by emission of light particles while slowly recoiling into the ϕ=180° side of the reaction plane. The ϕ=180° spectra are characteristic of emmision from an almost stationary source. The lack of agreement between the theory and the data could be due to the inability of the experimental arrangement to completely determine the reaction plane. Another explanation could be that the incompressibility constant, K, used in the HD calculation was 200 MeV whereas recent results[21] have shown that a much stiffer equation of state is required with K=380 MeV which would subtantially alter the calculations shown in Fig. 25 in the direction of producing more apparent forward motion.

Conclusions

We have studied both inclusive and triggered light particle emission in intermediate energy nucleus-nucleus collisions. The inclusive measurements were fitted using a moving source model and the resulting parameters were consistent with previously measured systematics of O- and Ne-induced reactions on heavy targets. Firestreak and hydrodynamics calculations reasonably reproduce the 92 MeV/nucleon ^{40}Ar + Au light particle spectra suggesting that thermal concepts play an important role in describing these collisions. The projectile-like fragment triggers varied from fragments that displayed an exponential spectrum consistent with emission from a thermal source to fragments that dominantly emerge at the projectile velocity. Light particles in coincidence with projectile velocity fragments near in mass to the projectile display an apparent velocity 30% slower than inclusive spectra. Light particles triggered by intermediate rapidity fragments as well as those triggered by PLFs that are not at the projectile velocity are similar to the inclusive

spectra. This similarity suggests that these particles have a common source. A momentum conservation model demonstrated that trivial kinematic effects are not strong for 30 MeV/nucleon ^{12}C + Au and 92 MeV/nucleon ^{40}Ar +Au. However, large effects predicted by the model were not seen in the data for the lighter system, ^{12}C + Al. These effects argue for a larger emitting system than the fireball geometry predicts.

This work was supported by the National Science Foundation under grant no. PHY-83-12245.

References

* Present address: Siemens Gammasonics, Des Plaines, IL 60018.

† Present address: Los Alamos National Laboratory, Los Alamos, NM 87545.

** Present address: CENBG Le Haut Vigneau, 33170 Gradignan, France.

1. B. Jakobsson, L. Carlen, P. Kristiansson, J. Krumlinde, A. Oskarsson, I. Otterlund, B. Schrøder, H.-A. Gustafsson, T. Johansson, H. Ryde, G. Tibell, J. P. Bondorf, G. Fài, A.O.T. Karvinen, O.B. Nielsen, M. Buenerd, J. Cole, D. Lebrun, J.M. Loiseaux, P. Martin, R. Ost, P. de Saintignon, C. Guet, E. Monnand, J. Mougey, H. Nifenecker, P. Perrin, J. Pinston, C. Ristori, and F. Schussler, Phys. Lett. 102B, 121 (1981).

2. J.B. Natowitz, M.N. Namboodiri, L. Adler, R.P. Schmitt, R.L. Watson, S. Simon, M. Berlanger, and R. Choudhury, Phys. Rev. Lett. 47, 1114 (1981).

3. G.D. Westfall, B.V. Jacak, N. Anantaraman, M.W. Curtin, G.M. Crawley, C.K. Gelbke, B. Hasselquist, W.G. Lynch, D.K. Scott, M.B. Tsang, M.J. Murphy, T.J.M. Symons, R. Legrain, T.J. Majors, Phys. Lett. 116B, 118 (1982) and references therein.

4. R.L. Auble, J.B. Ball, F.E. Bertrand, C.B. Fulmer, D.C. Hensley, I.L. Robinson, P.H. Stelson, C.Y. Wong, D.L. Hendrie, H.D. Holmgren, and J.D. Silk, Phys. Rev. C28, 1552 (1983).

5. B.V. Jacak, G.D. Westfall, C.K. Gelbke, L.H. Harwood, W.G. Lynch, D.K. Scott, H. Stöcker, M.B. Tsang, and T.J.M. Symons, Phys. Rev. Lett. 51, 1846 (1983).

6. R. Glasow, G.Gaul, B. Ludewigt, R. Santo, H. Ho, W. Kühn, U. Lynen and W.F.J. Müller, Phys. Lett. 120B, 71 (1983).

7. G.D. Westfall, Z.M. Koenig, B.V. Jacak. L.H. Harwood, G.M. Crawley, M.W. Curtin, C.K. Gelbke, B. Hasselquist, W.G. Lynch, A.D. Panagiotou, D.K. Scott, H. Stöcker, and M.B. Tsang, Phys. Rev. C29, 861 (1984).

8. D.J. Fields, W.G. Lynch, C.B. Chitwood, C.K. Gelbke, M.B. Tsang, H. Utsunomiya, and J. Aichelin, MSU Cyclotron Laboratory Preprint MSUCL 471, (1984).

9. V. Borrel, D. Guerreau, J. Galin, B. Gatty, D. Jacquet, and X. Tarrago, Z. Phys. A314, 191 (1983).

10. J. Mougey, R. Ost, M. Buenerd, J. Cole, C. Guet, D. Lebrun, J. M. Loiseaux, P. Martin, M. Maurel, E. Monnand, H. Nifenecker, P. Perrin, J. Pinston, C. Ristori, P. de Saintignon, F. Schussler, L. Carlen, B. Jakobsson, A. Oskarsson, I. Otterlund, B. Schrøder, H.-A. Gustafsson, T. Johansson, H. Ryde, J.P. Bondorf, O.B. Nielsen, and G. Tybell, Phys. Lett. 105B, 25 (1981).

11. F. Rami, J.P. Coffin, G. Guillaume, B. Heusch, P. Wagner, A. Fahli, and P. Fintz, report CRN/PN.8407 (1984).

12. B.V. Jacak, H. Stöcker, and G.D. Westfall, Phys. Rev. C29, 1744 (1984).

13. H.A. Gustafsson, H.H. Gutbrod, B. Kolb, H. Löhner, B. Ludewigt, A.M. Poskanzer, T. Renner, H. Riedesel, H.G. Ritter, A. Warwick, F. Weik, and H. Wieman, LBL Preprint LBL-17678, (1984) and Phys. Rev. Lett. 18, 1590 (1984).

14. G. Buchwald, private communication and H. Stöcker, L.P. Csernai. G. Graebner, G. Buchwald, H. Kruse, R.Y. Cusson, J.A. Maruhn, and W. Greiner, Phys. Rev. C25, 1873 (1982).

15. J. Gosset. J.I. Kapusta, and G.D. Westfall, Phys. Rev. C18, 844 (1978).

16. L.D. Landau and E.M. Lifshitz, Statistical Physics, Addison-Wesley, New York, 109 (1969).

17. J. Gosset, H.H. Gutbrod, W.G. Meyer, A.M. Poskanzer, A. Sandoval, R. Stock, and G.D. Westfall, Phys. Rev. C16, 629 (1977).

18. A.S. Goldhaber, Phys. Lett. 53B, 306 (1974).

19. Y.P. Viyogi, T.J.M. Symons, P. Doll, D.E. Greiner, H.H. Heckman, D.L. Hendrie, P.J. Lindstrom, J. Mahoney, D.K. Scott, H.J. Crawford, K. Van Bibber, G.D. Westfall, H. Wieman, C. MacParland, and C.K. Gelbke, Phys. Rev. Lett. 42, 33 (1979).

20. B.E. Hasselquist, Ph.D. Thesis, Michigan State University, unpublished (1984).

21. D. Hahn and H. Stöcker, MSUCL-505, (1985).

Figure Captions

Fig. 1. Inclusive spectra for p,d and t from 30 MeV/nucleon ^{12}C + Au and Al. The angles were 47° (•),56° (□),71° (Δ) and 90° (diamonds) for Au and 45° (•),56° (□),71° (Δ) and 90° (diamonds) for Al. The solid lines are moving source fits.

Fig. 2. Inclusive spectra for d and t from 30 MeV/nucleon ^{12}C + Au at 15° (+), 45° (•), 75° (□), 90° (⊠) and 105° (x).

Fig. 3. Inclusive spectra for p,d,t, ^{3}He and ^{4}He from 92 MeV/nucleon ^{40}Ar + Au. The solid lines correspond to moving source fits and the dot-dashed lines represent firestreak model calculations.

Fig. 4. Systematics of moving source parameters extracted from O- and Ne-induced reactions on heavy nuclei. The solid lines are to guide the eye and the dashed lines are fireball model calculations. Present results for ^{12}C- and ^{40}Ar-induced reactions are given in open symbols.

Fig. 5. Proton production cross sections from moving source fits. The solid line is a line drawn through the O- and Ne-induced results. The dashed and dot-dashed lines are scaled as described in the text for C- and Ar-induced reactions, respectively.

Fig. 6. Inclusive light particle spectra from 92 MeV/nucleon ^{40}Ar + Au at 45,67.5 and 90°. The solid lines are hydrodynamics calculations with thermal decay and the dot-dashed lines are firestreak model calculations. The hydrodynamics calculations have arbitrary normalizations listed in the text.

Fig. 7. Inclusive spectra for intermediate rapidity fragments (IRFs) for 30 MeV/nucleon ^{12}C + Al and Au at 25°.

Fig. 8. Proton spectra from 30 MeV/nucleon ^{12}C + Al triggered by intermediate rapidity fragments (IRFs). The spectra were measured at 45° (•),56° (□),71° (Δ) and 90° (diamonds). The solid lines represent moving source fits and the dot-dashed lines show momentum conservation model calculations as described in the text.

Fig. 9. Deuteron spectra from 30 MeV/nucleon ^{12}C + Al triggered by intermediate rapidity fragments (IRFs). The spectra were measured at 45° (•),56° (□),71° (Δ) and 90° (diamonds). The solid lines represent moving source fits and the dot-dashed lines show momentum conservation model calculations as described in the text.

Fig. 10. Triggered light particle spectra from 30 MeV/nucleon ^{12}C + Au at 47° (•),56° (□),71° (Δ) and 90° (diamonds). In (a) and (b) the proton spectra are triggered by intermediate rapidity fragments (IRFs) and projectile-like fragments (PLFs) respectively. In (c) and (d) the deuteron spectra are triggered by IRFs and PLFs respectively. The solid lines are moving source calculations and the dot-dashed lines are the momentum conservation model as described in the text.

Fig. 11. Inclusive spectra for intermediate rapidity fragments (IRFs) from 92 MeV/nucleon ^{40}Ar + Au at 30°. The solid lines are to guide the eye.

Fig. 12. Inclusive and intermediate rapidity fragment (IRF) triggered spectra for protons from 92 MeV/nucleon ^{40}Ar + Au at 45° (•), 67.5° (□) and 90° (⊠). The solid lines represent moving source fits and the dotted lines show the momentum conservation model as described in the text.

Fig. 13. Inclusive and intermediate rapidity fragment (IRF) triggered spectra for deuterons from 92 MeV/nucleon ^{40}Ar + Au at 45° (•), 67.5° (□) and 90° (⊠). The solid lines represent moving source fits and the dotted lines show the momentum conservation model as described in the text.

Fig. 14. Inclusive and intermediate rapidity fragment (IRF) triggered spectra for tritons from 92 MeV/nucleon ^{40}Ar + Au at 45° (•), 67.5° (□) and 90° (⊠). The solid lines represent moving source fits and the dotted lines show the momentum conservation model as described in the text.

Fig. 15. Inclusive and intermediate rapidity fragment (IRF) triggered spectra for ^{3}He from 92 MeV/nucleon ^{40}Ar + Au at 45° (•), 67.5° (□) and 90° (⊠). The solid lines represent moving source fits and the dotted lines show the momentum conservation model as described in the text.

Fig. 16. Inclusive and intermediate rapidity fragment (IRF) triggered spectra for ^{4}He from 92 MeV/nucleon ^{40}Ar + Au at 45° (•), 67.5° (□) and 90° (⊠). The solid lines represent moving source fits and the dotted lines show the momentum conservation model as described in the text.

Fig. 17. Ratios of moving source parameters extracted from triggered and inclusive proton and deuteron spectra from 30 MeV/nucleon ^{12}C + Al. The trigger in (a) and (c) is intermediate rapidity fragments (IRFs) and in (b) and (d) it is projectile like fragments (PLFs).

Fig. 18. Ratios of moving source parameters extracted from triggered and inclusive p, d, t, ^{3}He and ^{4}He spectra from 92 MeV/nucleon ^{40}Ar + Au. The trigger in (a) and (c) is intermediate rapidity fragments (IRFs) and in (b) and (d) it is projectile like fragments (PLFs).

Fig. 19. Inclusive spectra for projectile like fragments from 30 MeV/nucleon ^{12}C + Al (a) and Au (b) at 13°.

Fig. 20. Proton spectra from 30 MeV/nucleon ^{12}C + Al triggered by projectile like fragments (PLFs). The spectra were measured at 45° (•),56° (□),71° (Δ) and 90° (diamonds). The solid lines represent moving source fits and the dot-dashed lines show momentum conservation model calculations as described in the text.

Fig. 21. Inclusive spectra for projectile like fragments from 92 MeV/nucleon ^{40}Ar + Au at 13°.

Fig. 22. Inclusive and projectile like fragment (PLF) triggered spectra for protons from 92 MeV/nucleon ^{40}Ar + Au at 45° (•), 67.5° (□) and 90° (⊠). The solid lines represent moving source fits and the dotted lines show the momentum conservation model as described in the text.

Fig. 23. Inclusive and projectile like fragment (PLF) triggered spectra for deuterons from 92 MeV/nucleon ^{40}Ar + Au at 45° (•), 67.5° (□) and 90° (⊠). The solid lines represent moving source fits and the dotted lines show the momentum conservation model as described in the text.

Fig. 24. Inclusive and projectile like fragment (PLF) triggered spectra for tritons from 92 MeV/nucleon ^{40}Ar + Au at 45° (•), 67.5° (□) and 90° (⊠). The solid lines represent moving source fits and the dotted lines show the momentum conservation model as described in the text.

Fig. 25. Proton and deuteron spectra triggered by projectile like fragments from F to P from 92 MeV/nucleon ^{40}Ar + Au. The dot-dashed lines correspond to

non-azimuthally averaged hydrodynamics calculations for $\phi = 180°$ corresponding to angles in the reaction plane opposite the direction of the projectile.

Table 1. Detector angles and solid angles for the different experimental arrangements. All detectors are silicon except the array which was composed of CaF_2-plastic. Positive θ refers to the array side of the beam. Positive ϕ refers to upward out-of-plane.

Detector	Thicknesses (mm)	θ (°)	ϕ (°)	Solid Angle (msr)
30 MeV/nucleon ^{12}C+Al,Au				
PLF	.8,5,5	-13.0	0.0	4.38
IRF	0.1,0.3,5	-25.0	0.0	6.89
Array[1]	2,170	47,56,71,90	6.5	14.9
Array[2]	2,170	45,56,71,90	6.5	14.9
92 MeV/nucleon ^{40}Ar+Au				
PLF	0.8,5,5,5,5	-13.0	0.0	24.7
IRF[3]	0.8,0.8,5,5,5	-30.0	+10.0	16.0
IRF[4]	0.1,0.3,5	-30.0	-10.0	14.0
Array	2,170	45.0,67.5,90.0	0.0	12.0

[1]Scintillator Array for the Au Target.
[2]Scintillator Array for the Al target.
[3]High energy stack.
[4]Low energy stack.

Table 2. Representative dynamic ranges and energy cut-offs for particle detectors.

Telescope	Particle	Lower Cut-off (MeV/nucleon)	Upper Cut-off (MeV/nucleon)
30 MeV/nucleon			
Array	p, ^{4}He	18	160
PLF	Li	14	59
	C	20	87
IRF	Li	4	40
	O	7	69
92 MeV/nucleon			
Array	Same as above		
PLF	Li	14	85
	Ar	35	225
IRF,high	Li	14	75
	O	24	131
IRF,low	Li	4	40
	O	7	69

Table 3. Moving source parameters for inclusive light particle spectra.

Particle	Temperature τ (MeV)	Cross Section σ (mb)	Velocity β (c)
30 MeV/nucleon ^{12}C+Al			
p	9.5±0.2	774.± 38.	0.139±0.047
d	8.4±0.4	510.± 75.	0.130±0.007
t	7.0±0.2	760.±143.	0.140±0.003
30 MeV/nucleon ^{12}C+Au			
p	9.3±0.1	1200.± 32.	0.121±0.003
d	9.3±0.1	697.± 59.	0.100±0.005
t	9.2±0.6	600.±131.	0.092±0.005
92 MeV/nucleon ^{40}Ar+Au			
p	21.4±0.2	22600.±246.	0.205±0.002
d	21.6±0.2	13600.±223.	0.181±0.003
t	19.5±0.3	7827.±217.	0.152±0.002
^{3}He	29.4±0.2	2540.± 35.	0.218±0.002
^{4}He	25.9±0.3	3960.±111.	0.194±0.002

Table 4. Moving source parameters for light particle coincidence spectra triggered on IRFs.

Case	Trigger	Temperature τ (MeV)	Cross Section σ (mb)	Velocity β (c)
30 MeV/nucleon ^{12}C+Al => p				
	Li	9.4±0.2	17.± 1.	0.130±0.004
	Be	9.6±0.2	6.± 1.	0.127±0.002
	B	10.1±0.2	5.± 1.	0.141±0.004
	C	10.2±0.2	4.± 1.	0.125±0.002
30 MeV/nucleon ^{12}C+Al => d				
	Li	8.4±0.7	10.± 3.	0.130±0.017
	Be	8.6±0.4	4.± 1.	0.117±0.007
	B	8.6±0.4	4.± 1.	0.133±0.003
	C	8.1±0.4	4.± 1.	0.109±0.005
30 MeV/nucleon ^{12}C+Au => p				
	Li-C	10.1±0.1	50.± 4.	0.142±0.009
30 MeV/nucleon ^{12}C+Au => d				
	Li-C	10.0±0.8	37.± 6.	0.128±0.009
92 MeV/nucleon ^{40}Ar+Au => p				
	Li	23.0±0.6	8351.±192.	0.188±0.004
	Be	23.6±0.5	2312.± 62.	0.180±0.003
	B	23.5±0.6	1612.± 48.	0.178±0.005
	C	22.6±0.9	923.± 43.	0.182±0.008
	N	21.7±1.4	405.± 24.	0.169±0.009
92 MeV/nucleon ^{40}Ar+Au => d				
	Li	23.6±0.2	5271.±154.	0.171±0.010
	Be	23.8±0.6	1439.± 64.	0.161±0.004
	B	24.8±0.7	984.± 40.	0.172±0.004
	C	24.0±0.8	549.± 23.	0.156±0.007
	N	25.8±1.7	224.± 16.	0.159±0.008
92 MeV/nucleon ^{40}Ar+Au => t				
	Li	19.8±0.5	3497.±155.	0.137±0.004
	Be	20.4±1.0	894.± 71.	0.135±0.006
	B	23.0±1.5	642.± 50.	0.144±0.007
	C	24.6±0.9	362.± 28.	0.138±0.023
	N	23.3±1.3	164.± 24.	0.133±0.017
92 MeV/nucleon ^{40}Ar+Au => ^{3}He				
	Li	34.3±1.3	910.± 52.	0.208±0.014
	Be	31.9±3.8	286.± 45.	0.223±0.021
	B	32.9±4.9	176.± 22.	0.178±0.035
	C	35.3±6.9	109.± 12.	0.159±0.059
92 MeV/nucleon ^{40}Ar+Au => ^{4}He				
	Li	25.2±1.0	1882.±158.	0.172±0.007
	Be	26.3±1.3	546.± 56.	0.183±0.006
	B	27.8±1.6	386.± 64.	0.197±0.012
	C	27.5±2.4	219.± 25.	0.199±0.013
	N	25.7±5.2	90.± 17.	0.152±0.035

Table 5. Moving source parameters for light particle spectra triggered by PLFs.

Case	Trigger	Temperature τ (MeV)	Cross Section σ (mb)	Velocity β (c)
30 MeV/nucleon ^{12}C+Al => p				
	Li	9.4±0.4	46.± 3.	0.127±0.002
	Be	10.1±0.1	21.± 1.	0.134±0.005
	B	10.4±0.5	22.± 2.	0.129±0.006
	C	10.2±0.6	24.± 2.	0.126±0.006
30 MeV/nucleon ^{12}C+Au => p				
	Li-B	9.7±0.4	94.± 8.	0.100±0.008
30 MeV/nucleon ^{12}C+Au => d				
	Li-B	12.4±0.7	29.± 6.	0.095±0.028
92 MeV/nucleon ^{40}Ar+Au => p				
	Li	21.8±0.3	9365.±264.	0.202±0.005
	Be	21.1±0.3	4458.±149.	0.190±0.006
	B	21.6±0.5	2928.± 97.	0.199±0.006
	C	21.0±0.6	1590.± 68.	0.192±0.007
	N	21.2±0.9	588.± 30.	0.192±0.008
	O	22.4±1.9	233.± 18.	0.187±0.018
	F-P	22.5±2.1	187.± 16.	0.145±0.016
92 MeV/nucleon ^{40}Ar+Au => d				
	Li	22.4±0.7	5115.±272.	0.183±0.006
	Be	21.6±0.7	2490.±143.	0.173±0.005
	B	21.2±0.9	1667.± 96.	0.177±0.005
	C	21.2±1.2	921.± 72.	0.183±0.010
	N	20.3±1.2	372.± 32.	0.166±0.010
	O	20.5±2.2	153.± 23.	0.161±0.019
	F-P	24.6±3.3	88.± 11.	0.126±0.020
92 MeV/nucleon ^{40}Ar+Au => t				
	Li	18.9±0.9	3186.±264.	0.165±0.008
	Be	19.0±1.2	1462.±149.	0.159±0.009
	B	19.9±1.6	906.±103.	0.165±0.009
	C	19.2±1.8	569.± 89.	0.164±0.013
	N	20.3±1.6	197.± 30.	0.176±0.019
	O	15.9±2.3	130.± 25.	0.146±0.022
	F-P	24.9±3.9	64.± 17.	0.159±0.026

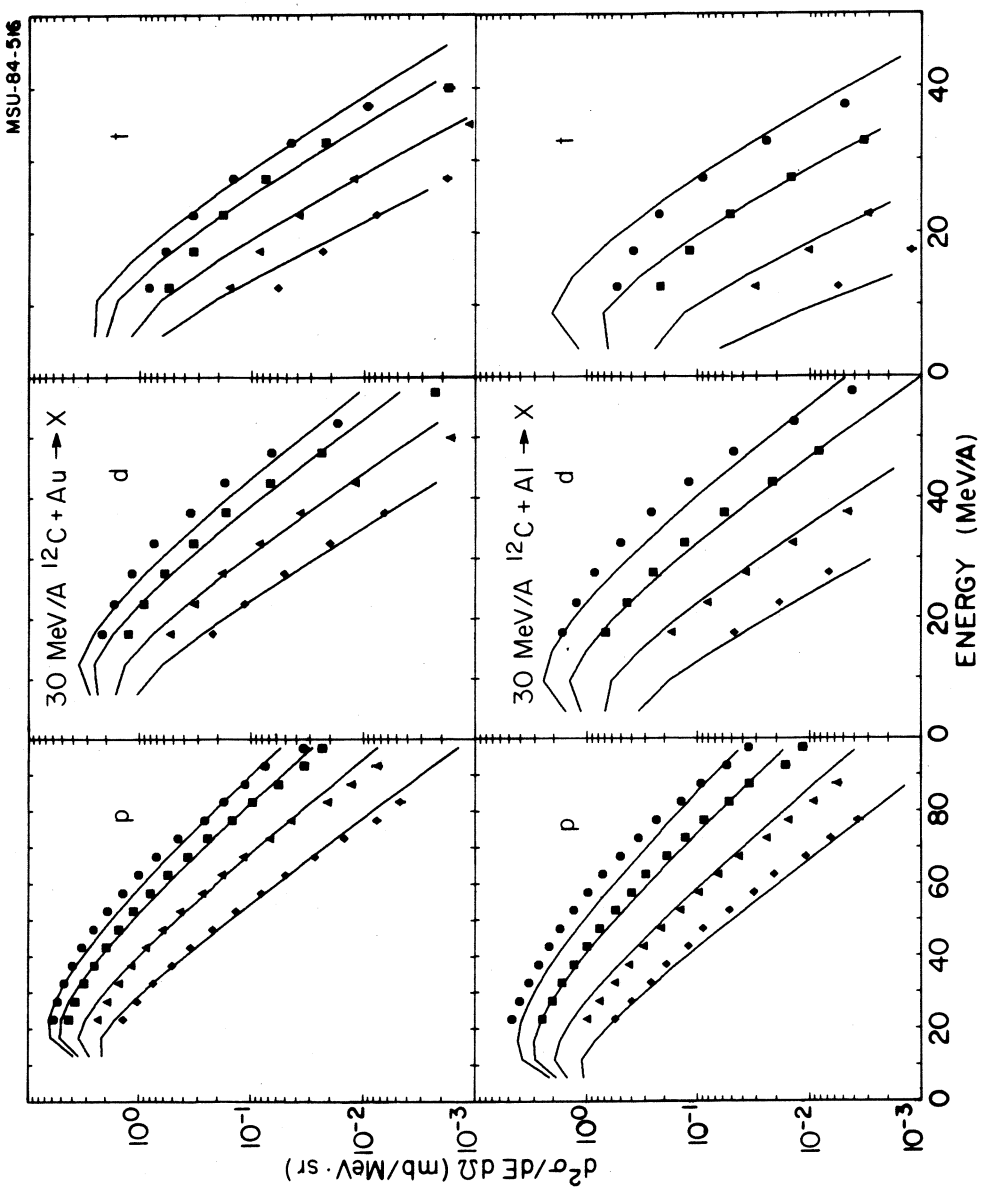
MSU-84-516
30 MeV/A ^{12}C + Au → X
30 MeV/A ^{12}C + Al → X
p
d
t
$d^2\sigma/dE\,d\Omega$ (mb/MeV · sr)
ENERGY (MeV/A)

Fig. 1

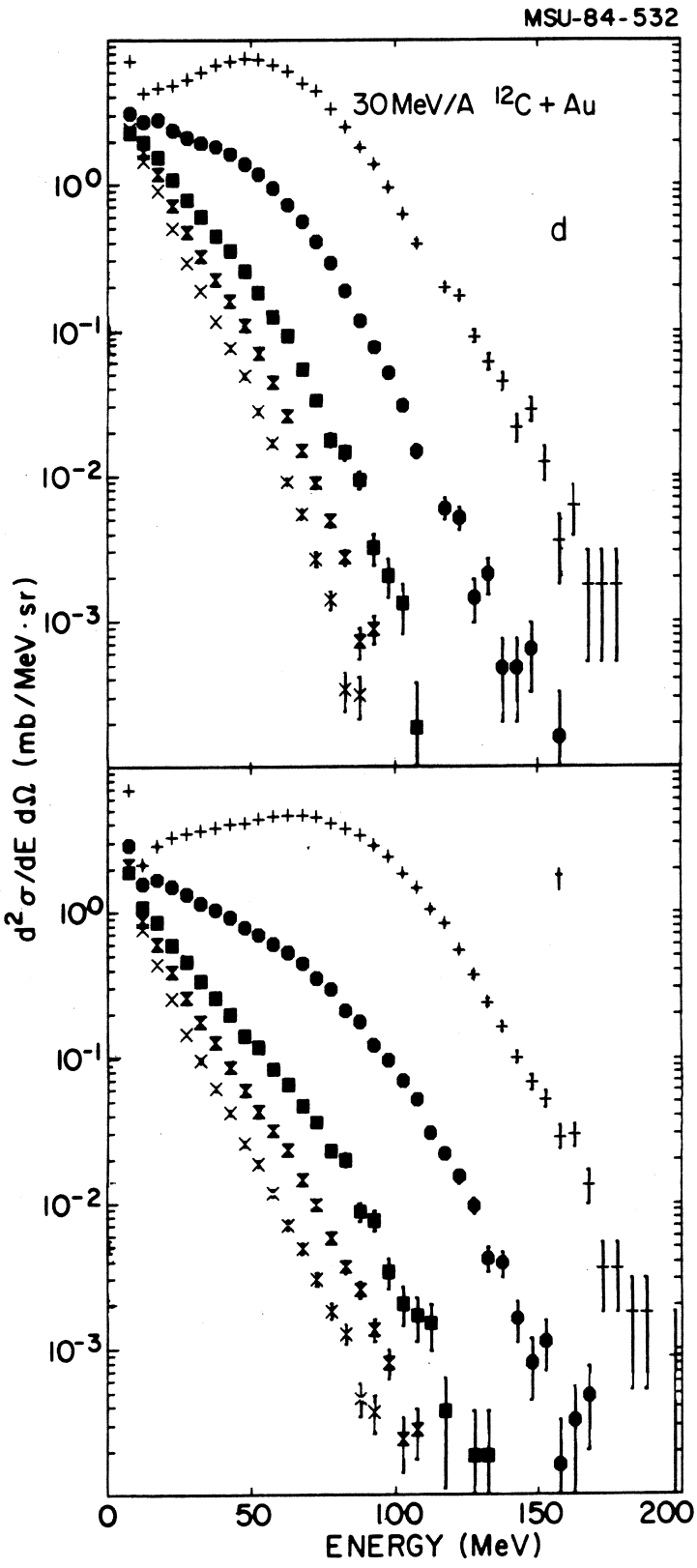
MSU-84-532
30MeV/A ^{12}C + Au
d
t
$d^2\sigma/dE\,d\Omega$ (mb/MeV·sr)
10^0
10^{-1}
10^{-2}
10^{-3}
0
50
100
150
200
ENERGY (MeV)

Fig. 2

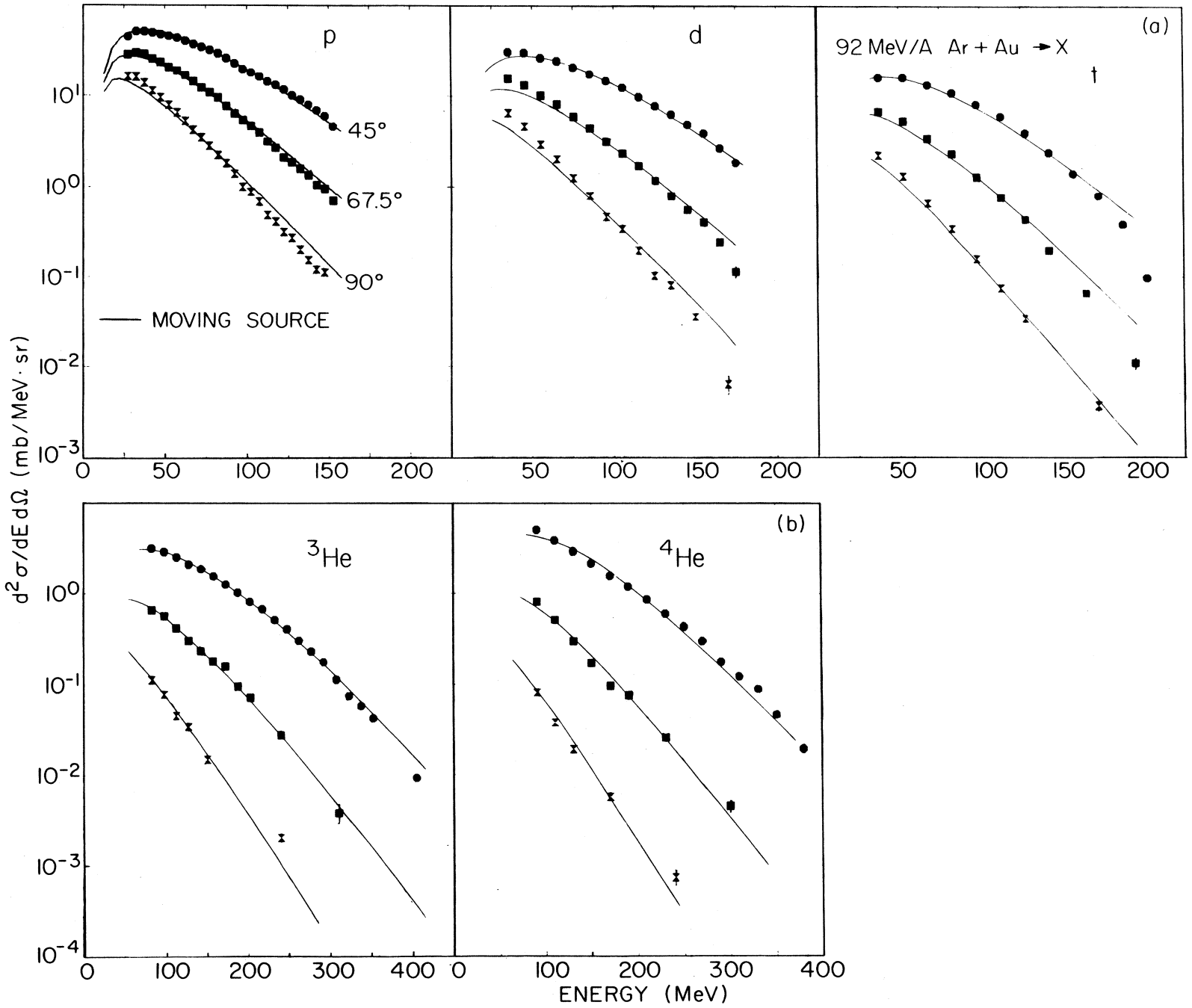
p
d
t
(a)
92 MeV/A Ar + Au → X
45°
67.5°
90°
MOVING SOURCE
^{3}He
^{4}He
(b)
$d^2\sigma/dE\,d\Omega$ (mb/MeV·sr)
ENERGY (MeV)

Fig. 3

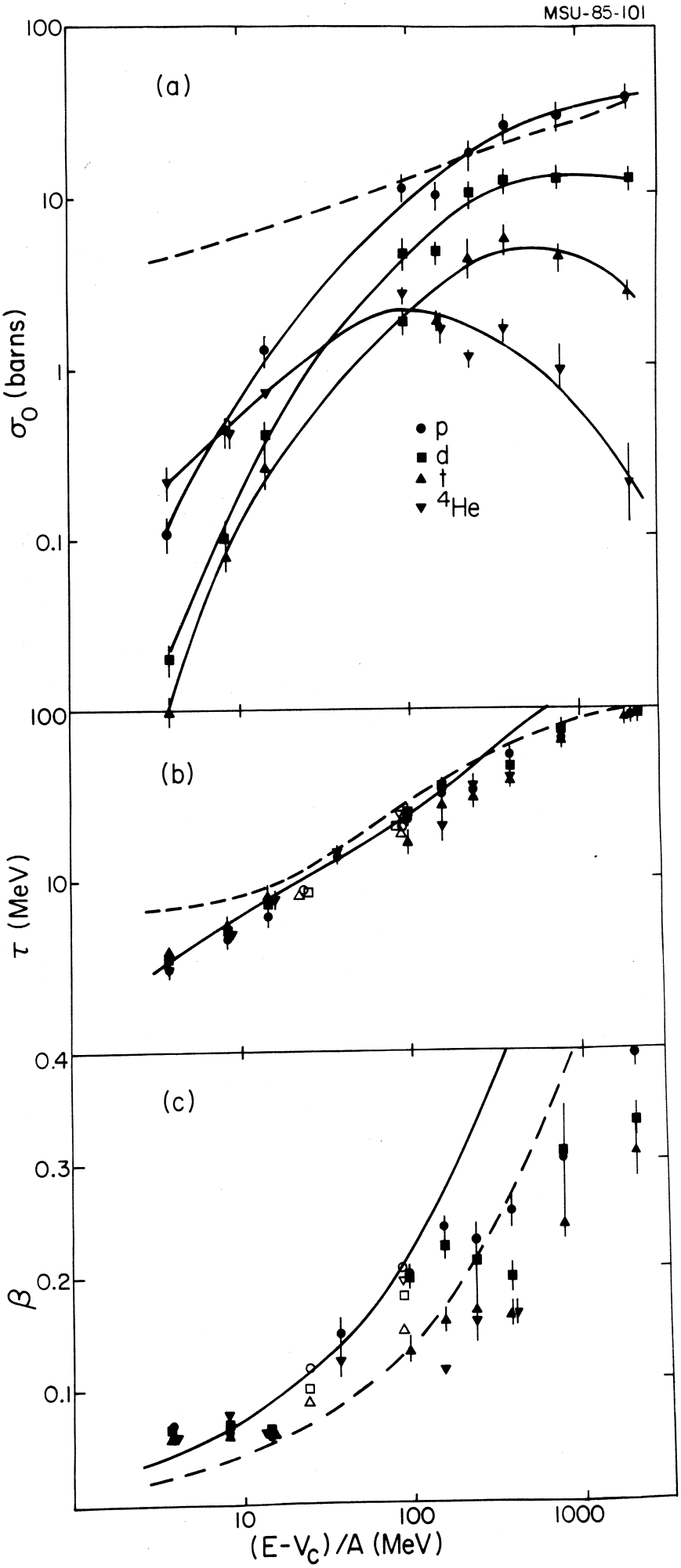
(a)
(b)
(c)
σ_0 (barns)
τ (MeV)
β
p
d
t
^{4}He
100
10
1
0.1
0.4
0.3
0.2
10
100
1000
$(E-V_c)/A$ (MeV)

Fig. 4

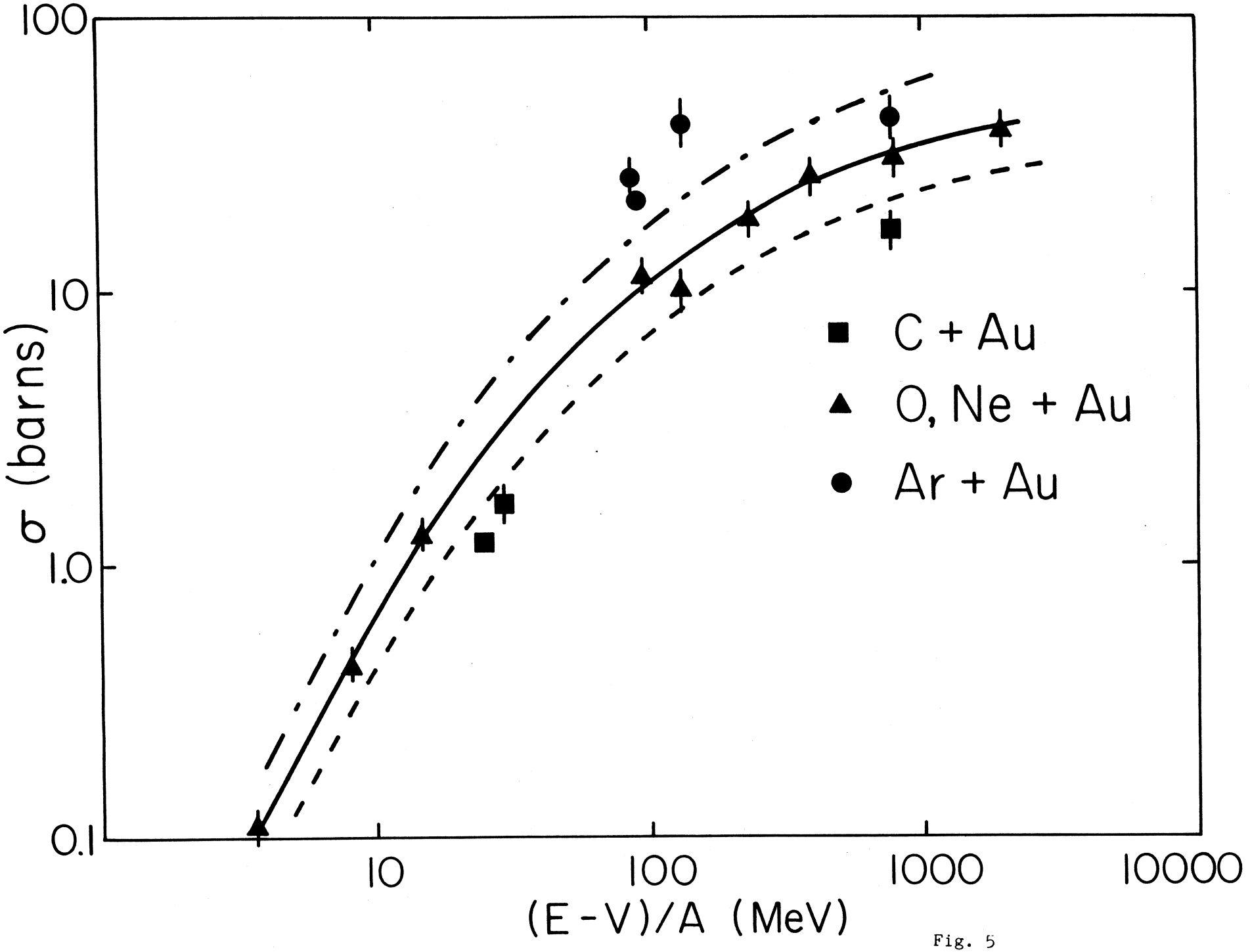

Fig. 5

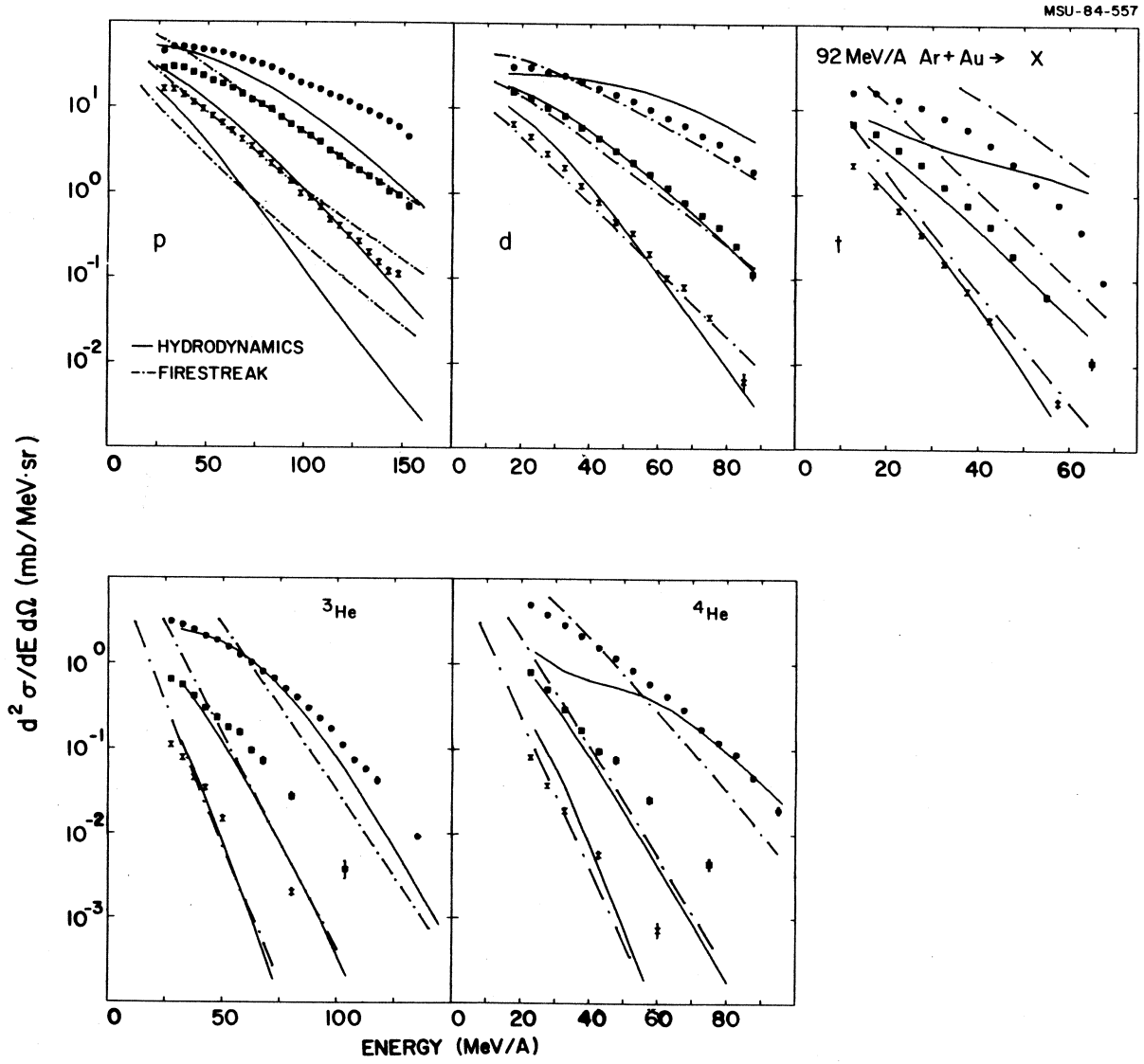
MSU-84-557
92 MeV/A Ar+Au → X
p
d
t
HYDRODYNAMICS
FIRESTREAK
^{3}He
^{4}He
$d^2\sigma/dE\,d\Omega$ (mb/MeV·sr)
ENERGY (MeV/A)

Fig. 6

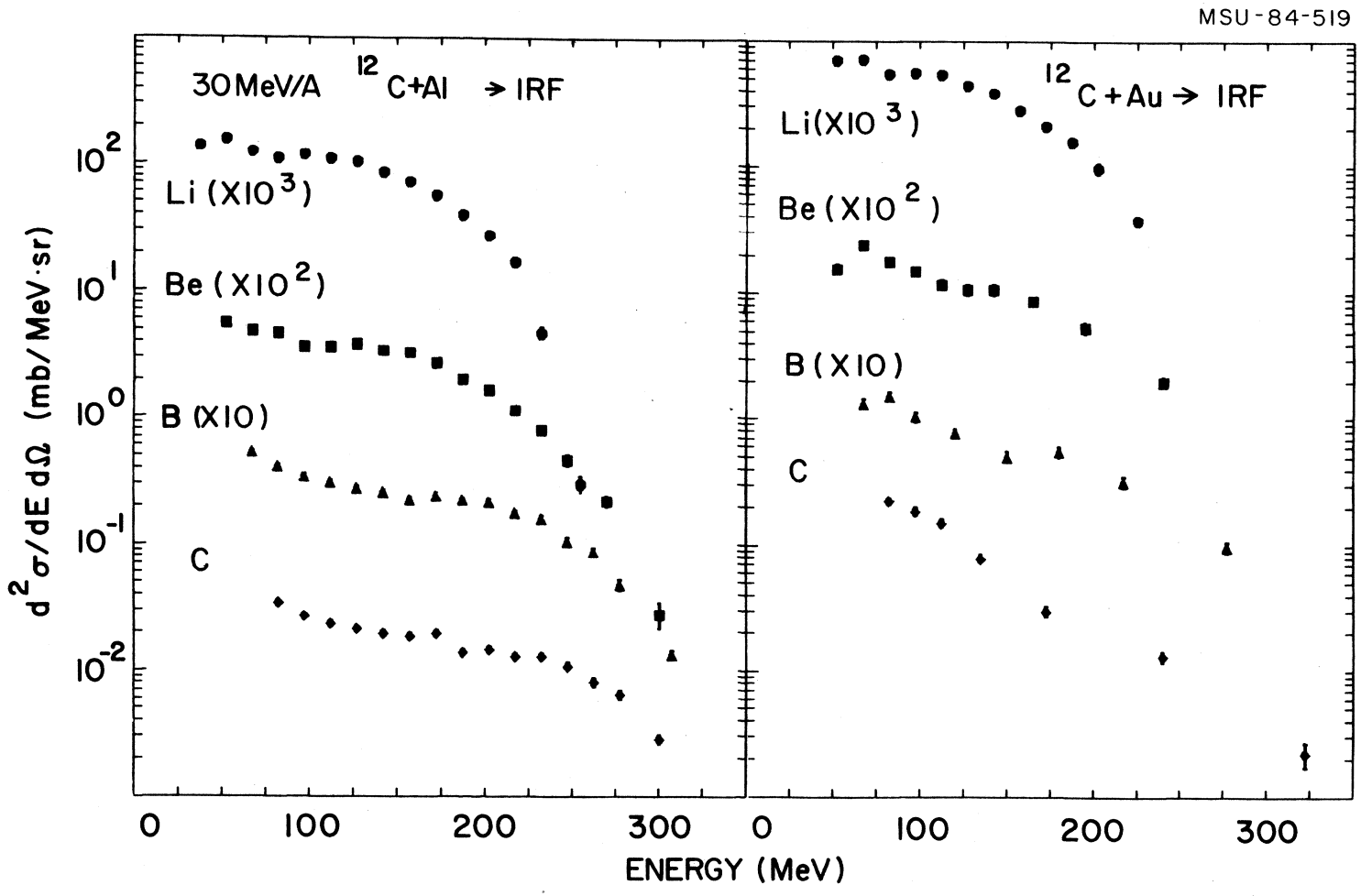
MSU-84-519
30MeV/A ^{12}C+Al → IRF
Li (X10^3)
Be (X10^2)
B (X10)
C
$d^2\sigma/dE\,d\Omega$ (mb/MeV·sr)
10^2
10^1
10^0
10^{-1}
10^{-2}
0
100
200
300
^{12}C + Au → IRF
Li(X10^3)
Be (X10^2)
B (X10)
C
0
100
200
300
ENERGY (MeV)

Fig. 7

MSU-84-495

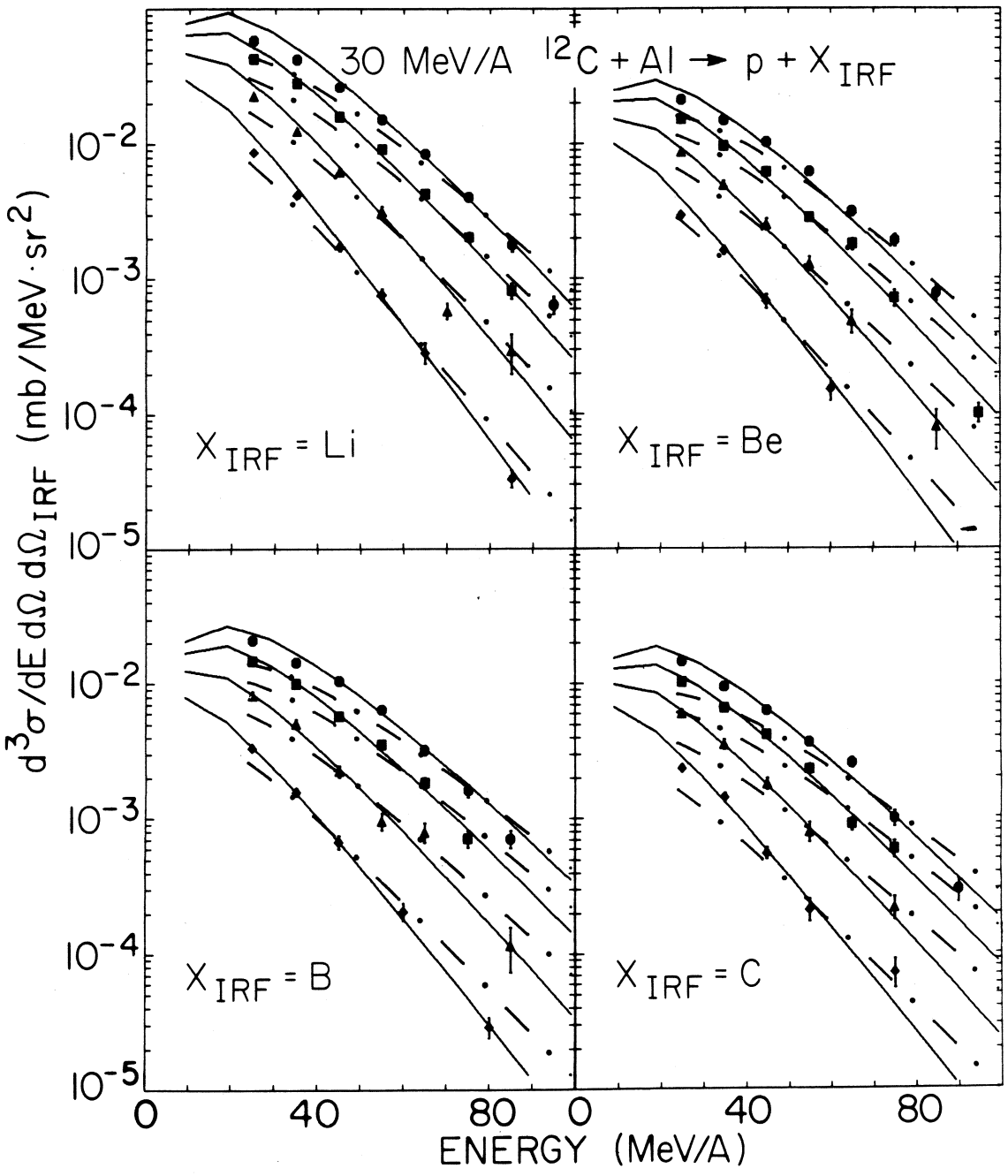

Fig. 8

MSU-84-498

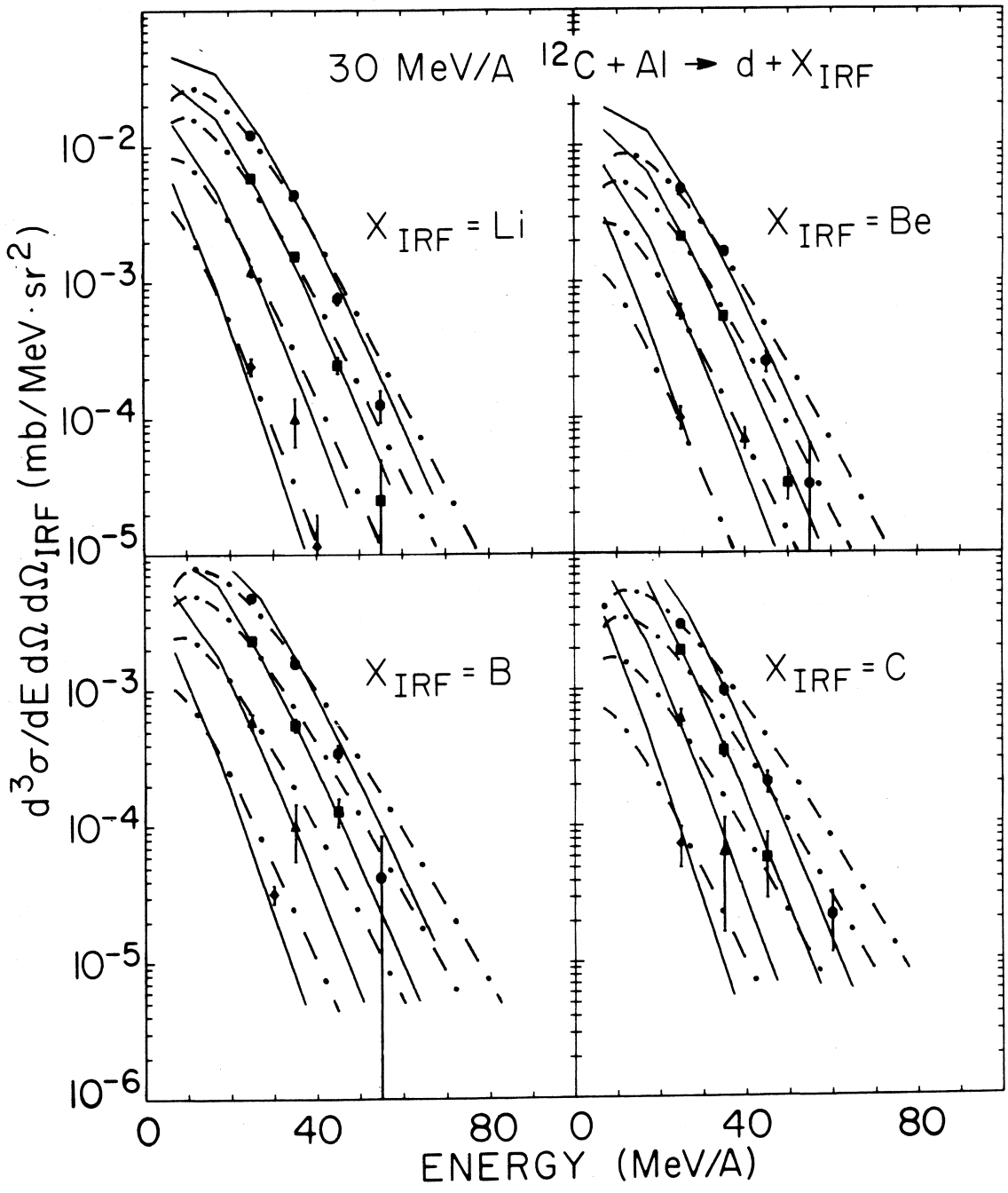

Fig. 9

MSU-84-497

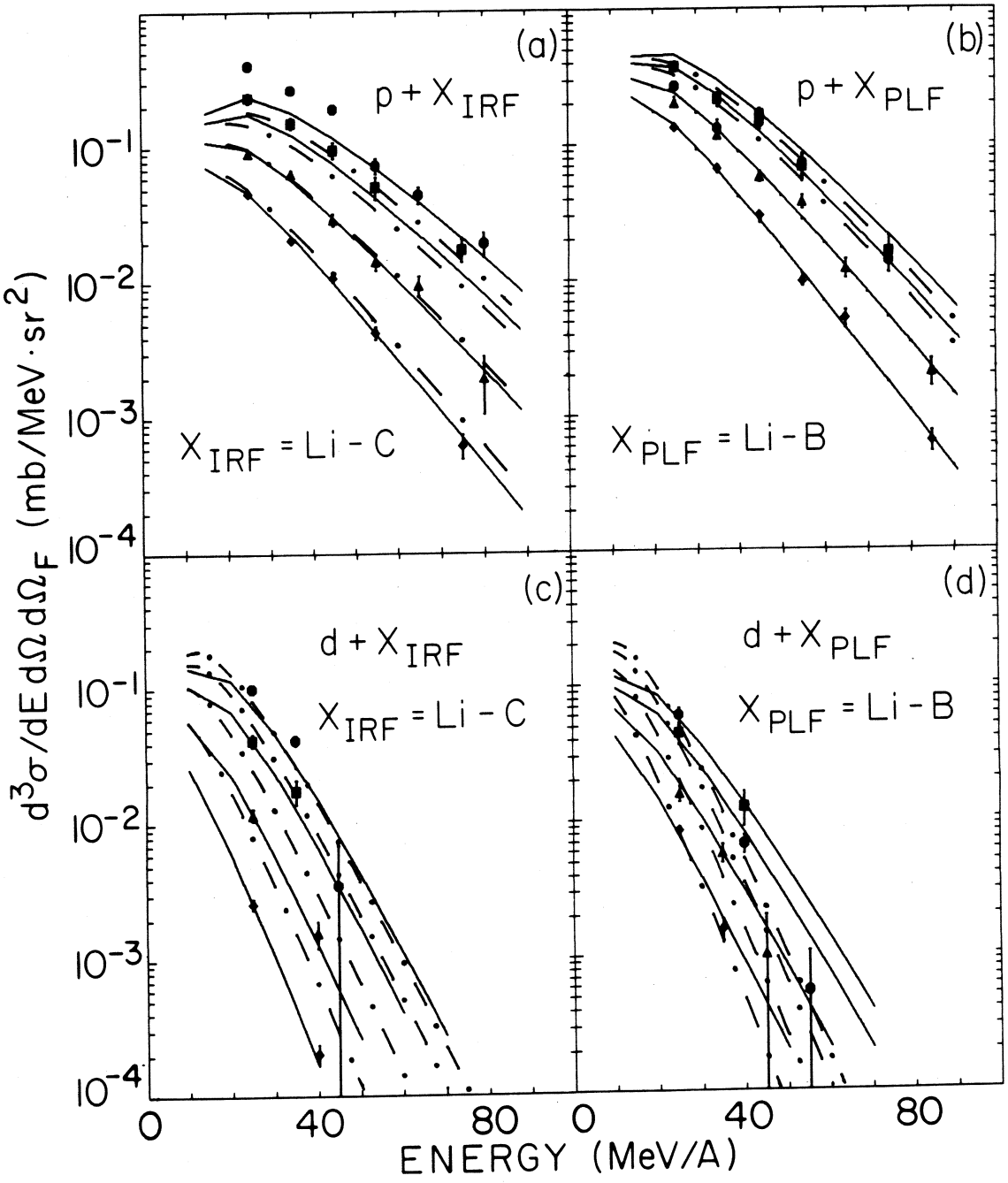

Fig. 10

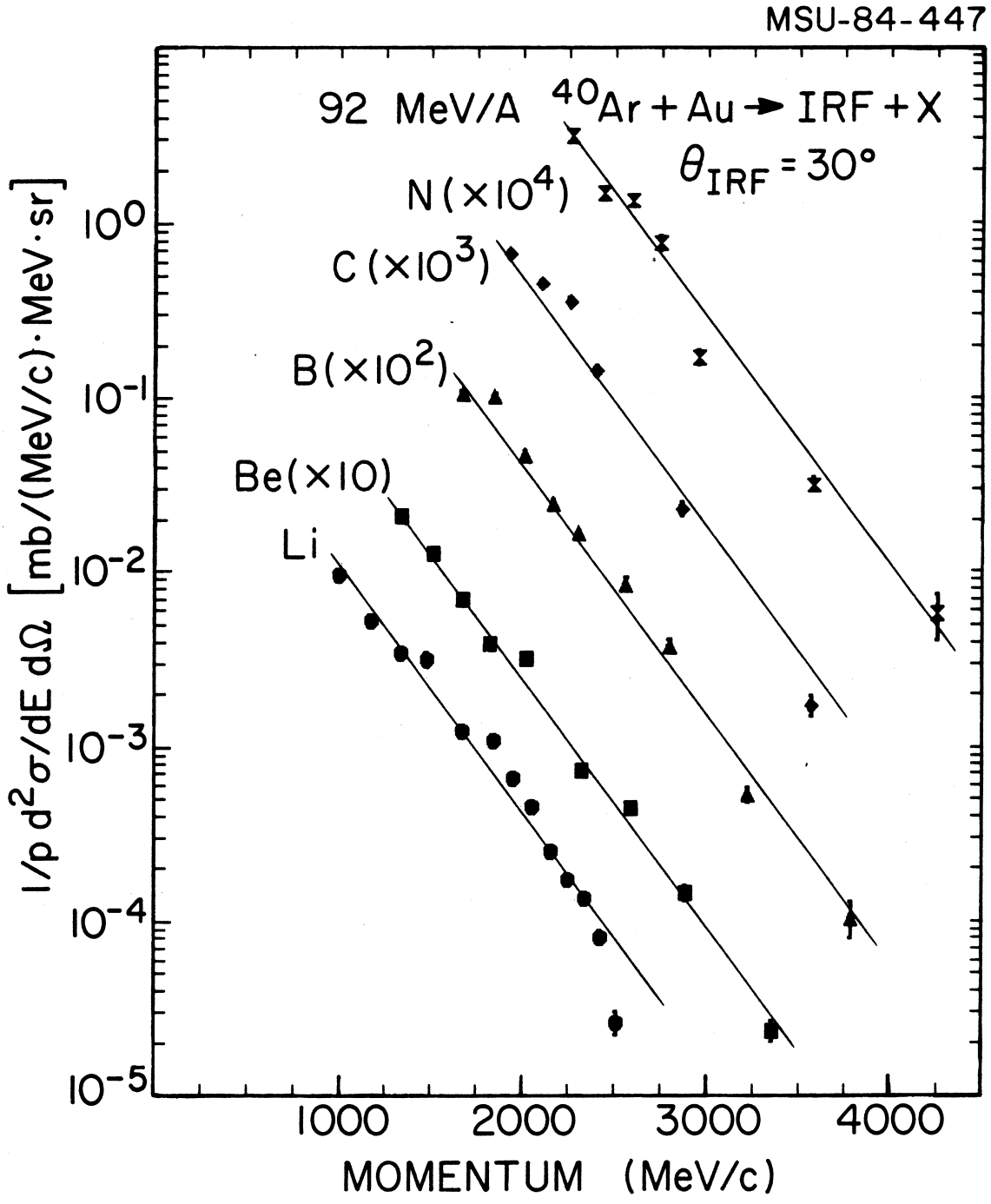
MSU-84-447
92 MeV/A ^{40}Ar + Au → IRF + X
θ_{IRF} = 30°
N(×10^4)
C(×10^3)
B(×10^2)
Be(×10)
Li
1/p d$^2\sigma$/dE dΩ [mb/(MeV/c)·MeV·sr]
10^0
10^{-1}
10^{-2}
10^{-3}
10^{-4}
10^{-5}
1000
2000
3000
4000
MOMENTUM (MeV/c)

Fig. 11

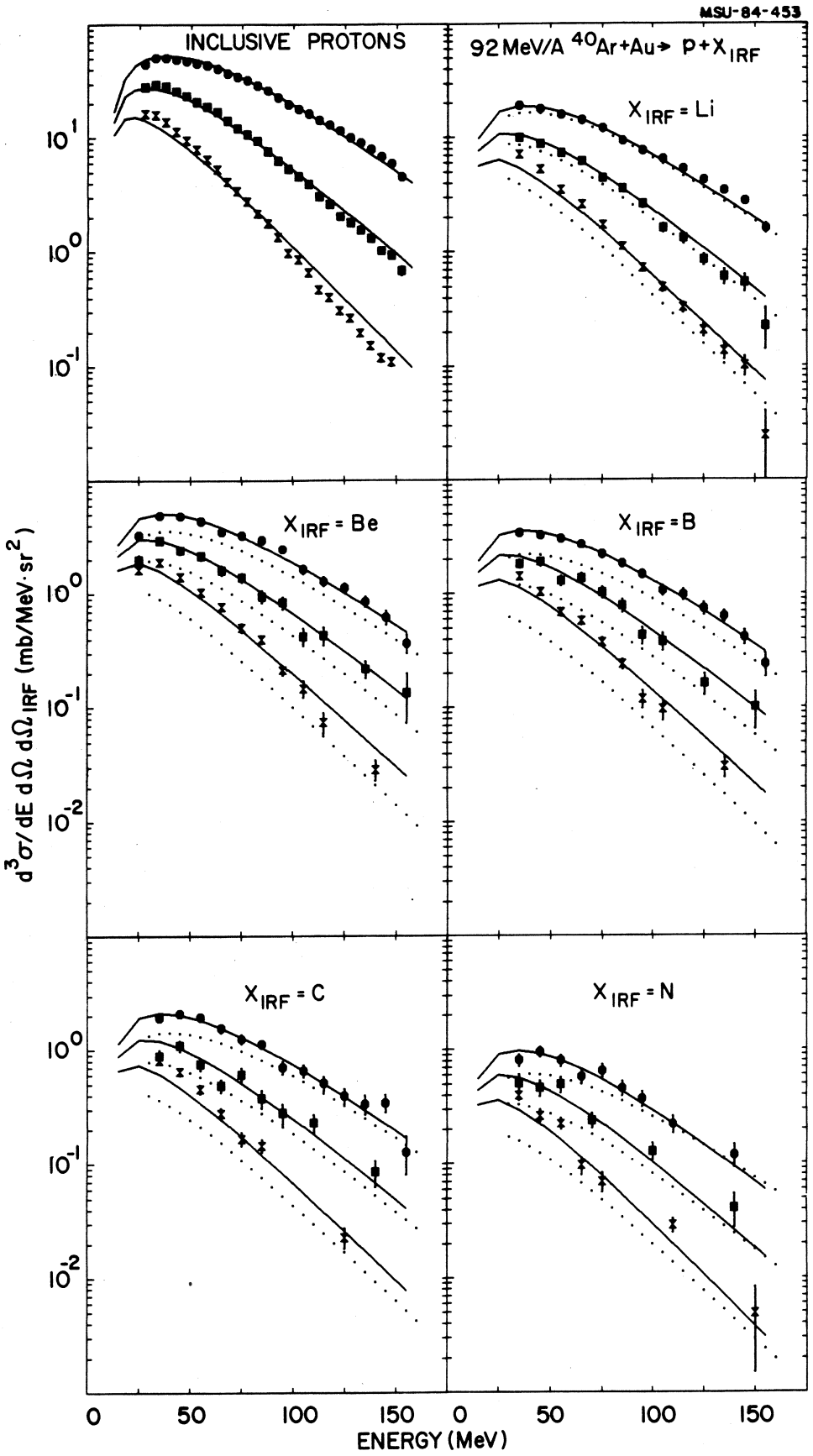
MSU-84-453
INCLUSIVE PROTONS
92 MeV/A ^{40}Ar+Au → p+X$_{IRF}$
X$_{IRF}$ = Li
X$_{IRF}$ = Be
X$_{IRF}$ = B
X$_{IRF}$ = C
X$_{IRF}$ = N
$d^3\sigma/dE\,d\Omega\,d\Omega_{IRF}$ (mb/MeV·sr^2)
ENERGY (MeV)
0
50
100
150
10^1
10^0
10^{-1}
10^{-2}

Fig. 12

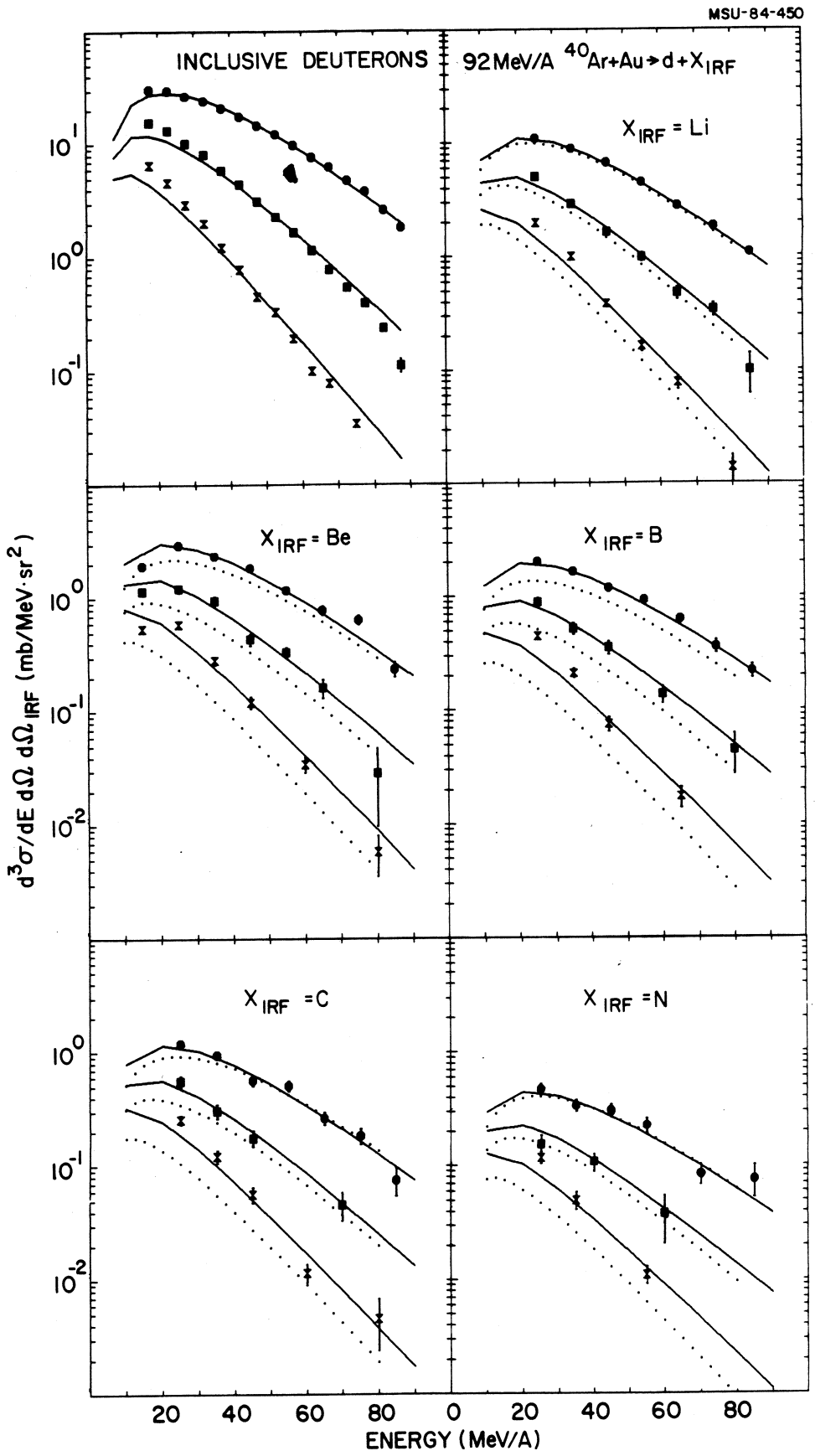
MSU-84-450
INCLUSIVE DEUTERONS
92MeV/A ^{40}Ar+Au→d+X$_{IRF}$
X$_{IRF}$ = Li
X$_{IRF}$ = Be
X$_{IRF}$ = B
X$_{IRF}$ = C
X$_{IRF}$ = N
$d^3\sigma/dE\, d\Omega\, d\Omega_{IRF}$ (mb/MeV·sr^2)
ENERGY (MeV/A)

Fig. 13

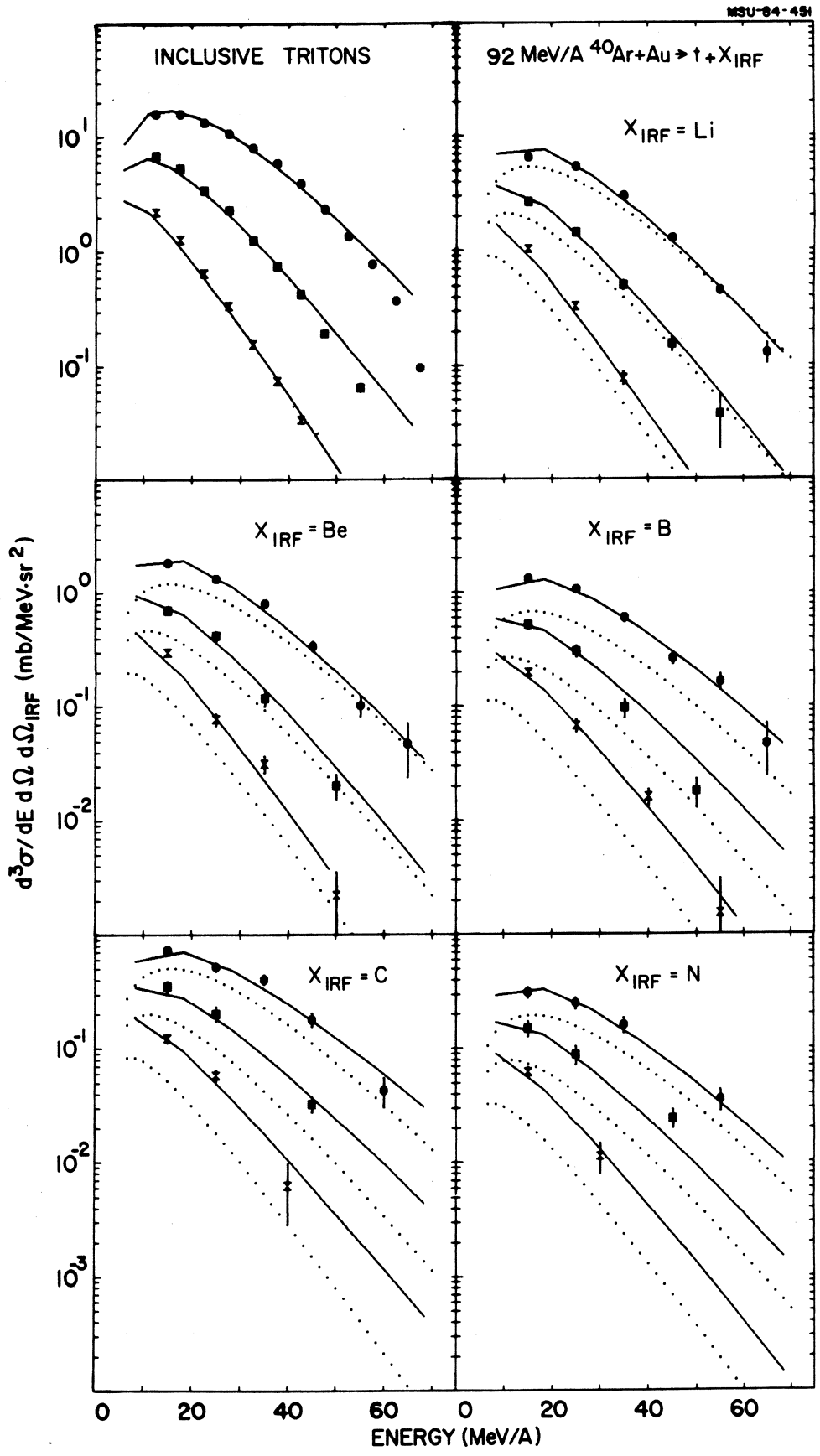
MSU-84-451
INCLUSIVE TRITONS
92 MeV/A ^{40}Ar+Au → t + X_{IRF}
X_{IRF} = Li
X_{IRF} = Be
X_{IRF} = B
X_{IRF} = C
X_{IRF} = N
$d^3\sigma/dE\,d\Omega\,d\Omega_{IRF}$ (mb/MeV·sr^2)
ENERGY (MeV/A)

Fig. 14

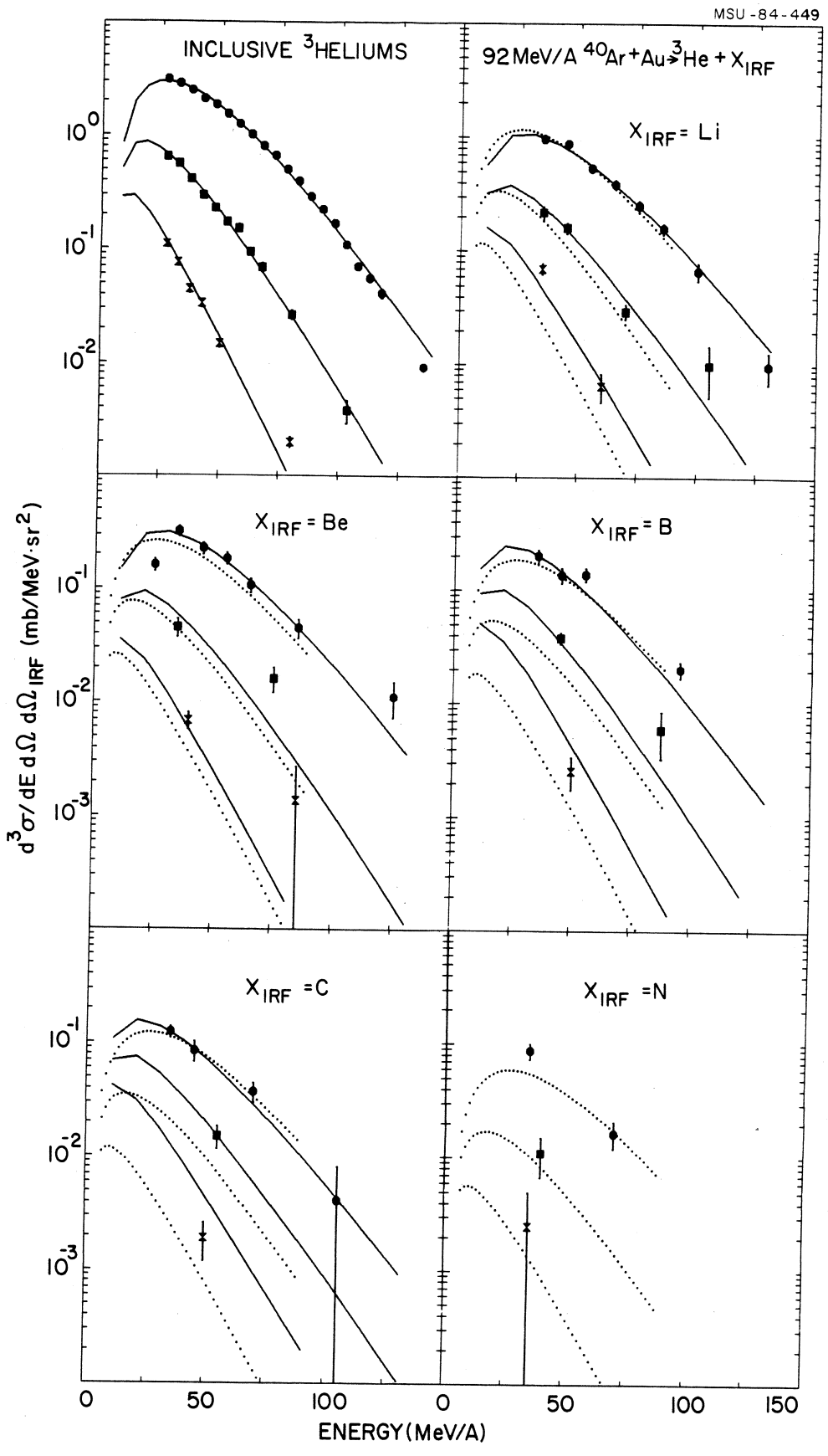
MSU-84-449
INCLUSIVE ^{3}HELIUMS
92 MeV/A ^{40}Ar+Au → ^{3}He + X_{IRF}
X_{IRF} = Li
X_{IRF} = Be
X_{IRF} = B
X_{IRF} = C
X_{IRF} = N
$d^3\sigma/dE\,d\Omega\,d\Omega_{IRF}$ (mb/MeV·sr^2)
ENERGY (MeV/A)
0
50
100
150
10^0
10^{-1}
10^{-2}
10^{-3}

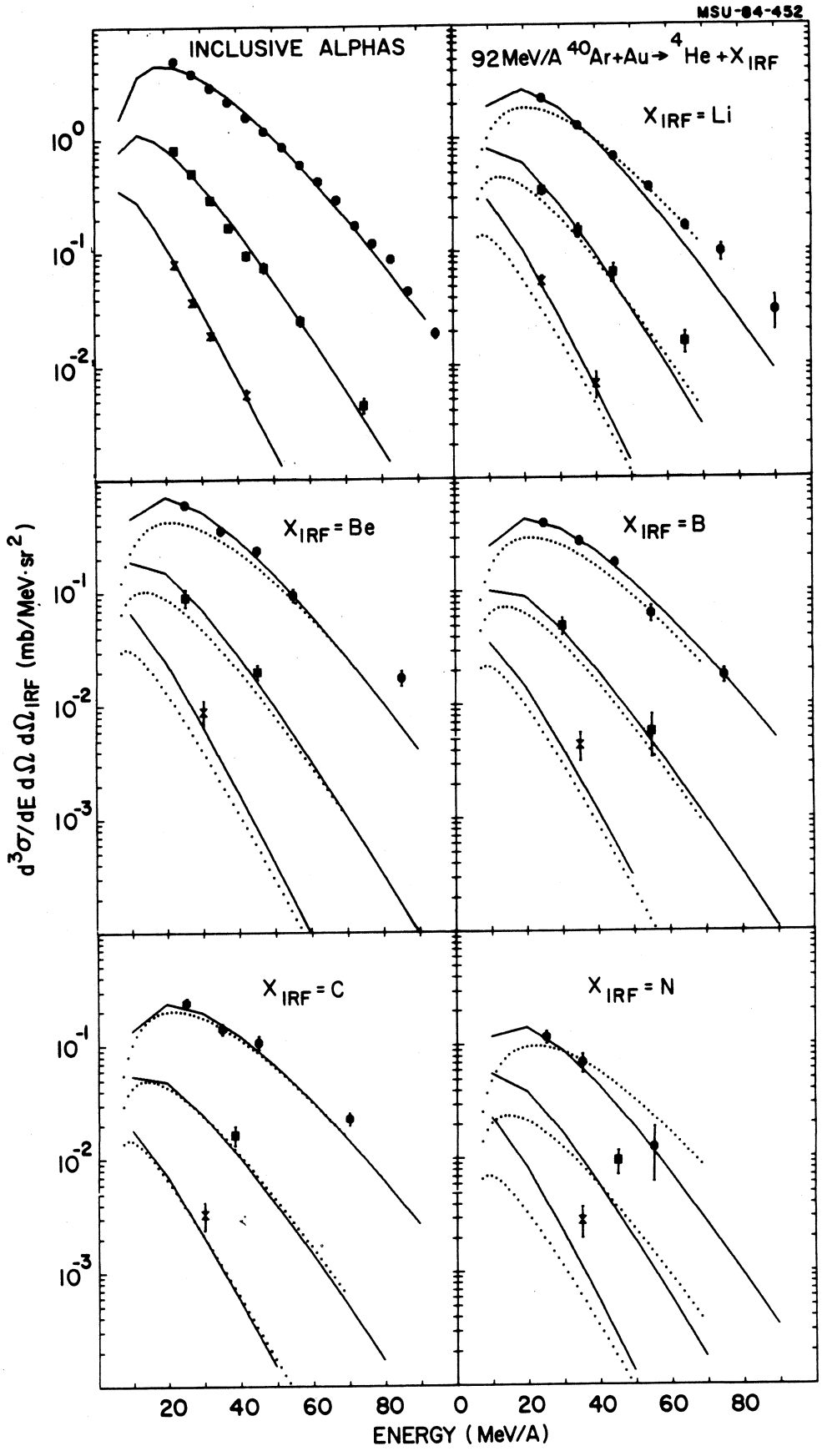
MSU-84-452
INCLUSIVE ALPHAS
92MeV/A ^{40}Ar+Au→ ^{4}He +X$_{IRF}$
X$_{IRF}$ = Li
X$_{IRF}$ = Be
X$_{IRF}$ = B
X$_{IRF}$ = C
X$_{IRF}$ = N
$d^3\sigma/dE\,d\Omega\,d\Omega_{IRF}$ (mb/MeV·sr^2)
ENERGY (MeV/A)

Fig. 16

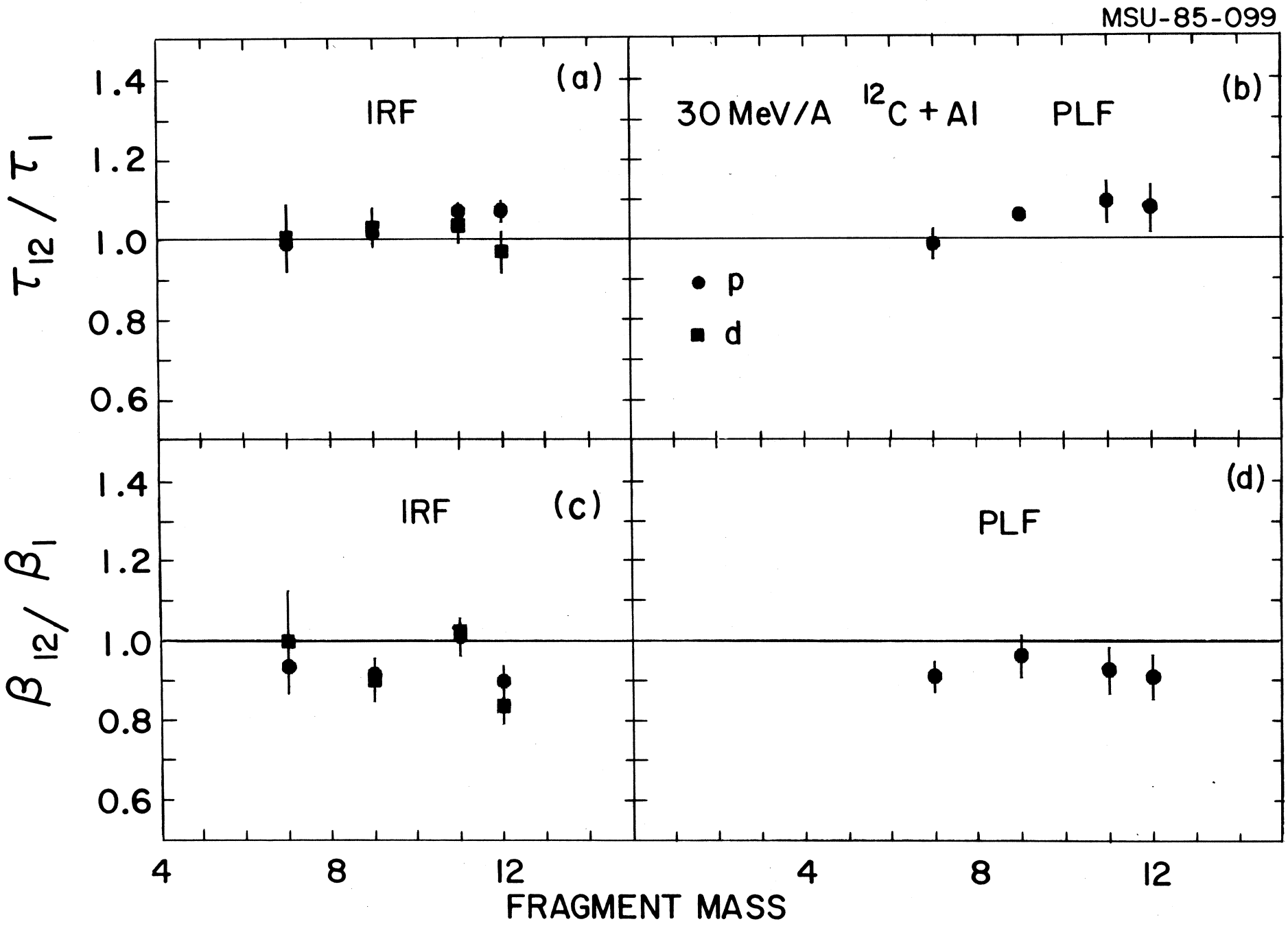
MSU-85-099
(a)
IRF
(b)
30 MeV/A ^{12}C + Al
PLF
p
d
(c)
IRF
(d)
PLF
τ_{12}/τ_1
β_{12}/β_1
1.4
1.2
1.0
0.8
0.6
4
8
12
FRAGMENT MASS

Fig. 17

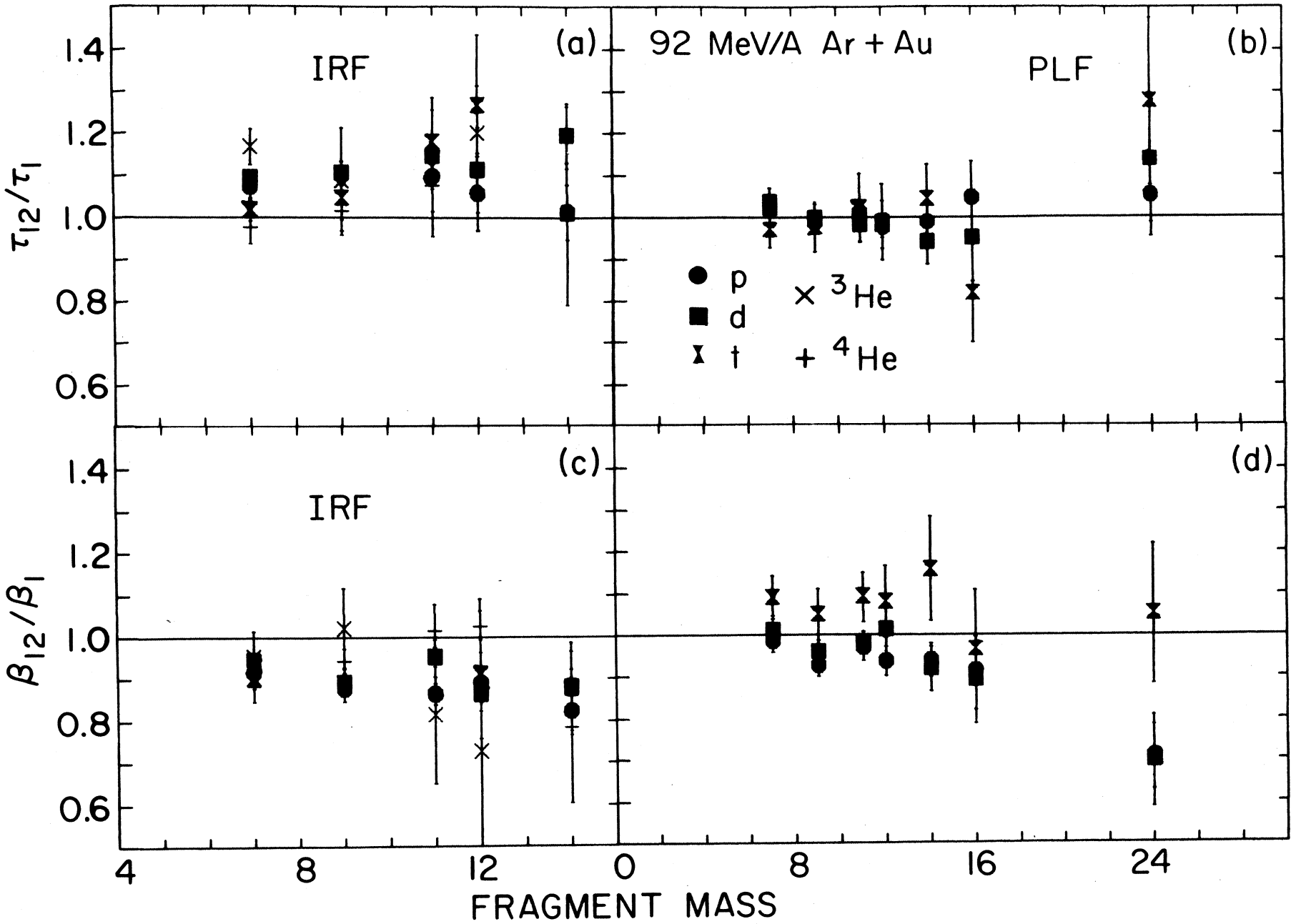
(a)
IRF
92 MeV/A Ar + Au
(b)
PLF
p
d
t
× 3He
+ 4He
(c)
IRF
(d)
τ12/τ1
β12/β1
1.4
1.2
1.0
0.8
0.6
4
8
12
0
8
16
24
FRAGMENT MASS

Fig. 18

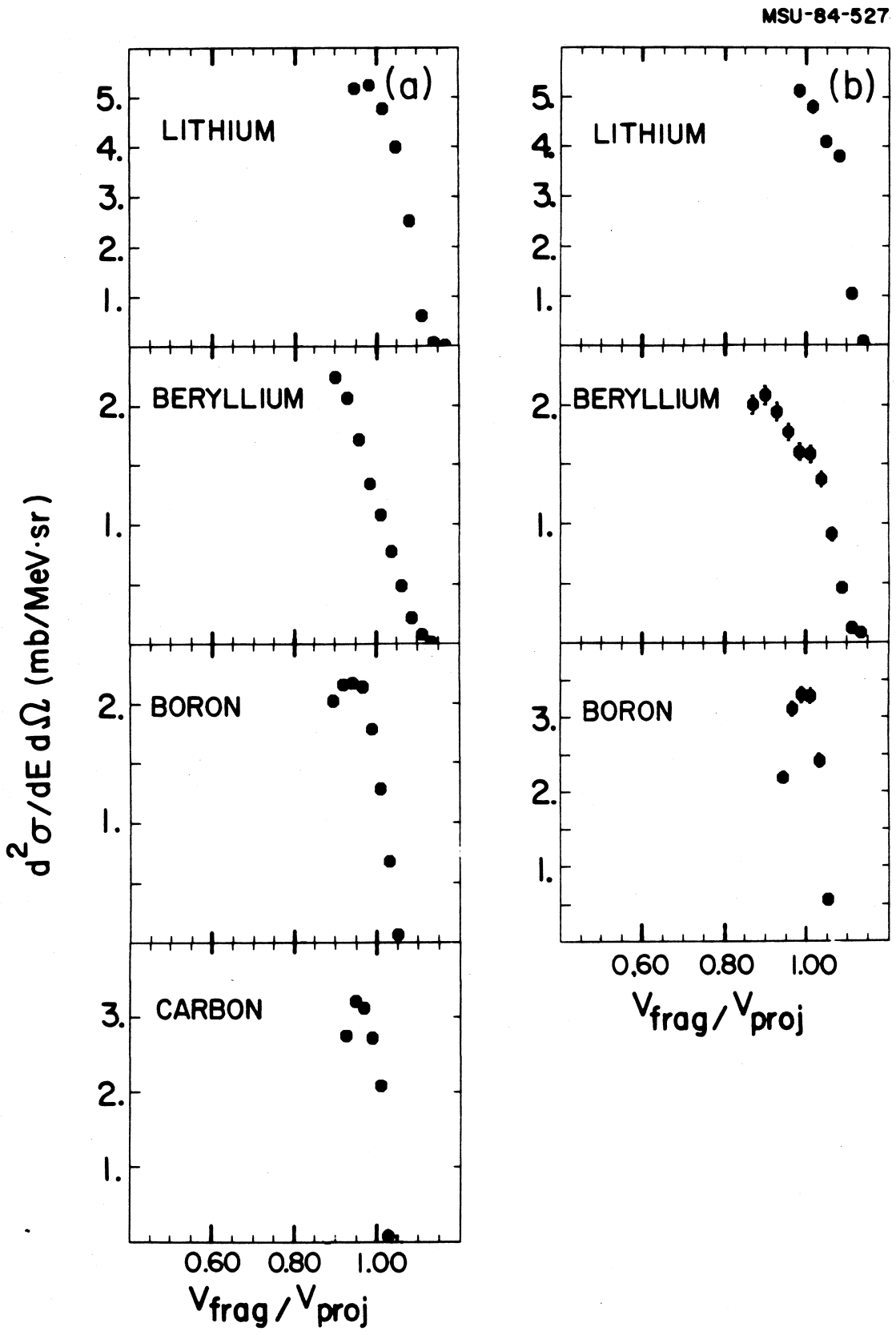
MSU-84-527
(a)
(b)
LITHIUM
BERYLLIUM
BORON
CARBON
d²σ/dE dΩ (mb/MeV·sr)
V_frag / V_proj
0.60
0.80
1.00

Fig. 19

MSU-84-496

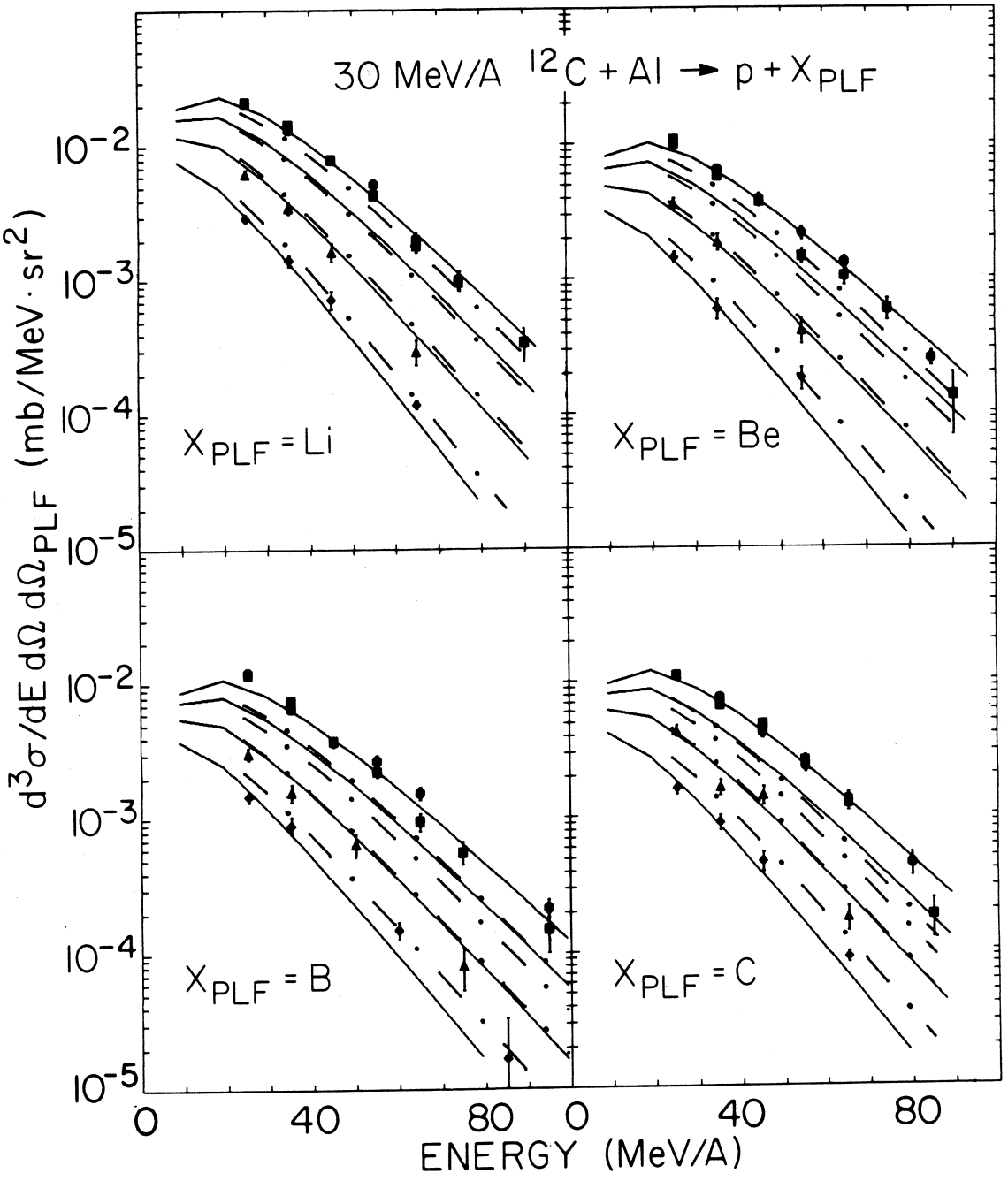

Fig. 20

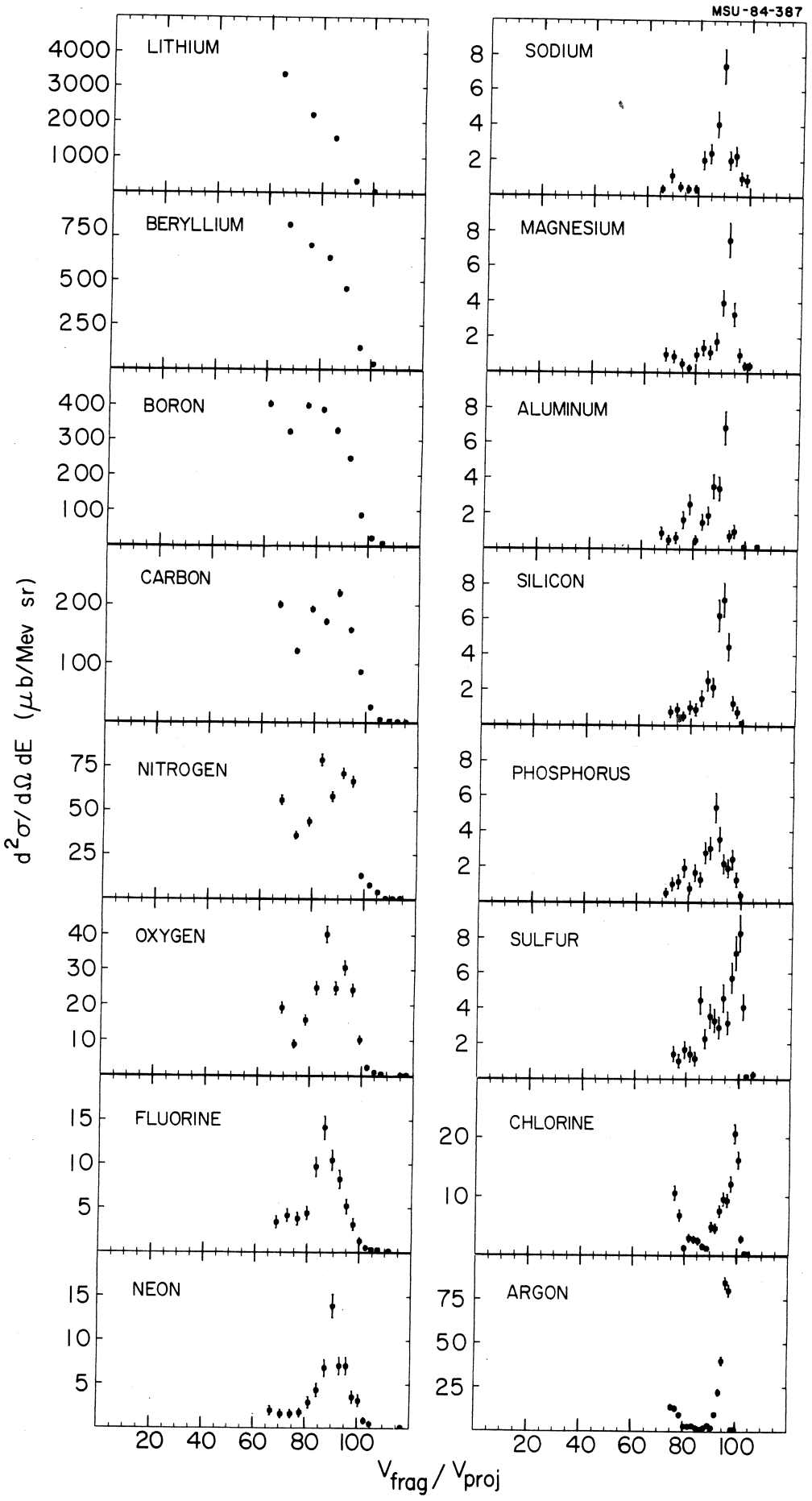
MSU-84-387
LITHIUM
BERYLLIUM
BORON
CARBON
NITROGEN
OXYGEN
FLUORINE
NEON
SODIUM
MAGNESIUM
ALUMINUM
SILICON
PHOSPHORUS
SULFUR
CHLORINE
ARGON
$d^2\sigma/d\Omega\,dE$ (μb/Mev sr)
V_{frag}/V_{proj}

Fig. 21

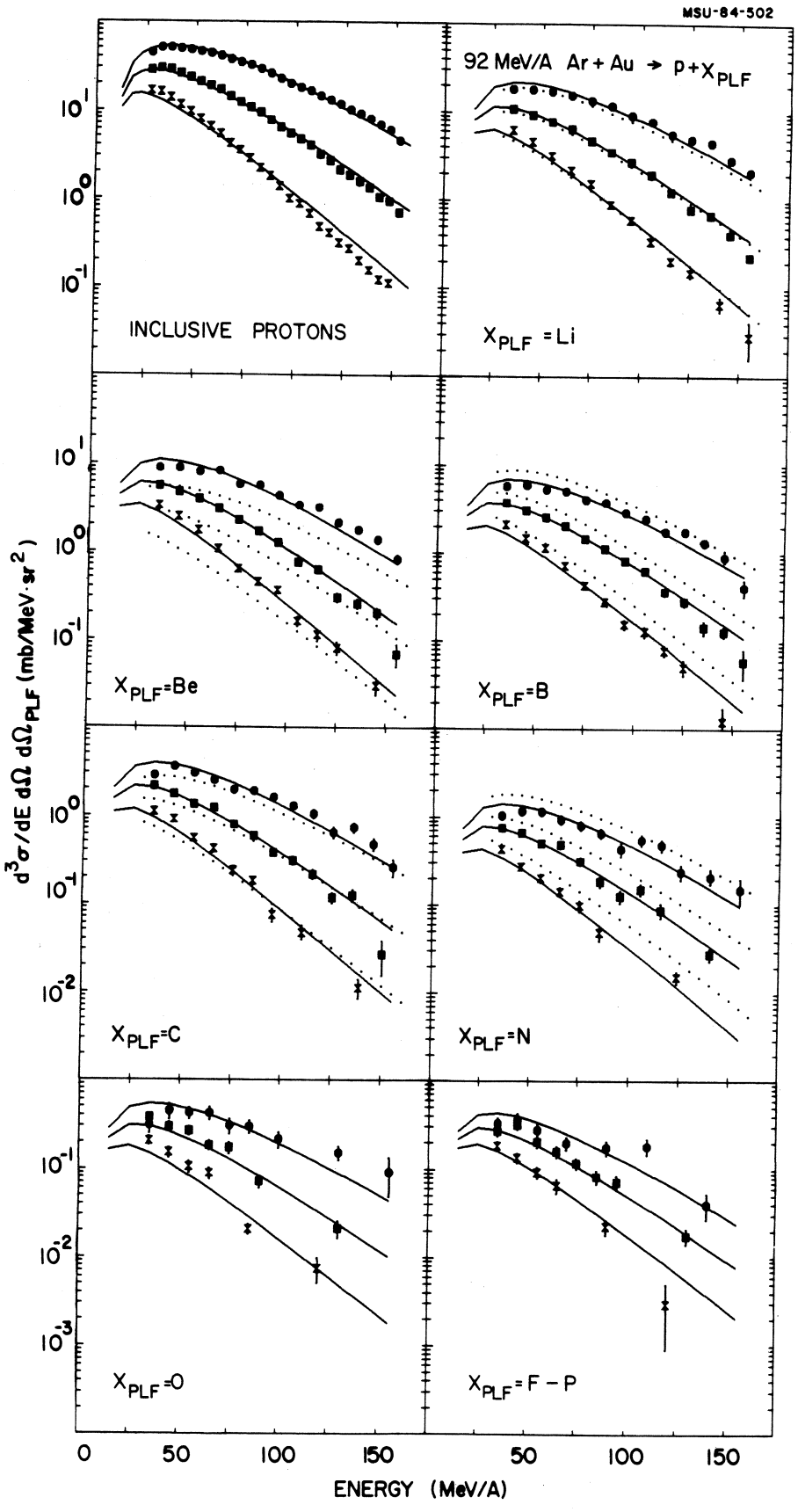
MSU-84-502
92 MeV/A Ar + Au → p + X_PLF
INCLUSIVE PROTONS
X_PLF = Li
X_PLF = Be
X_PLF = B
X_PLF = C
X_PLF = N
X_PLF = O
X_PLF = F - P
d³σ/dE dΩ dΩ_PLF (mb/MeV·sr²)
ENERGY (MeV/A)

Fig. 22

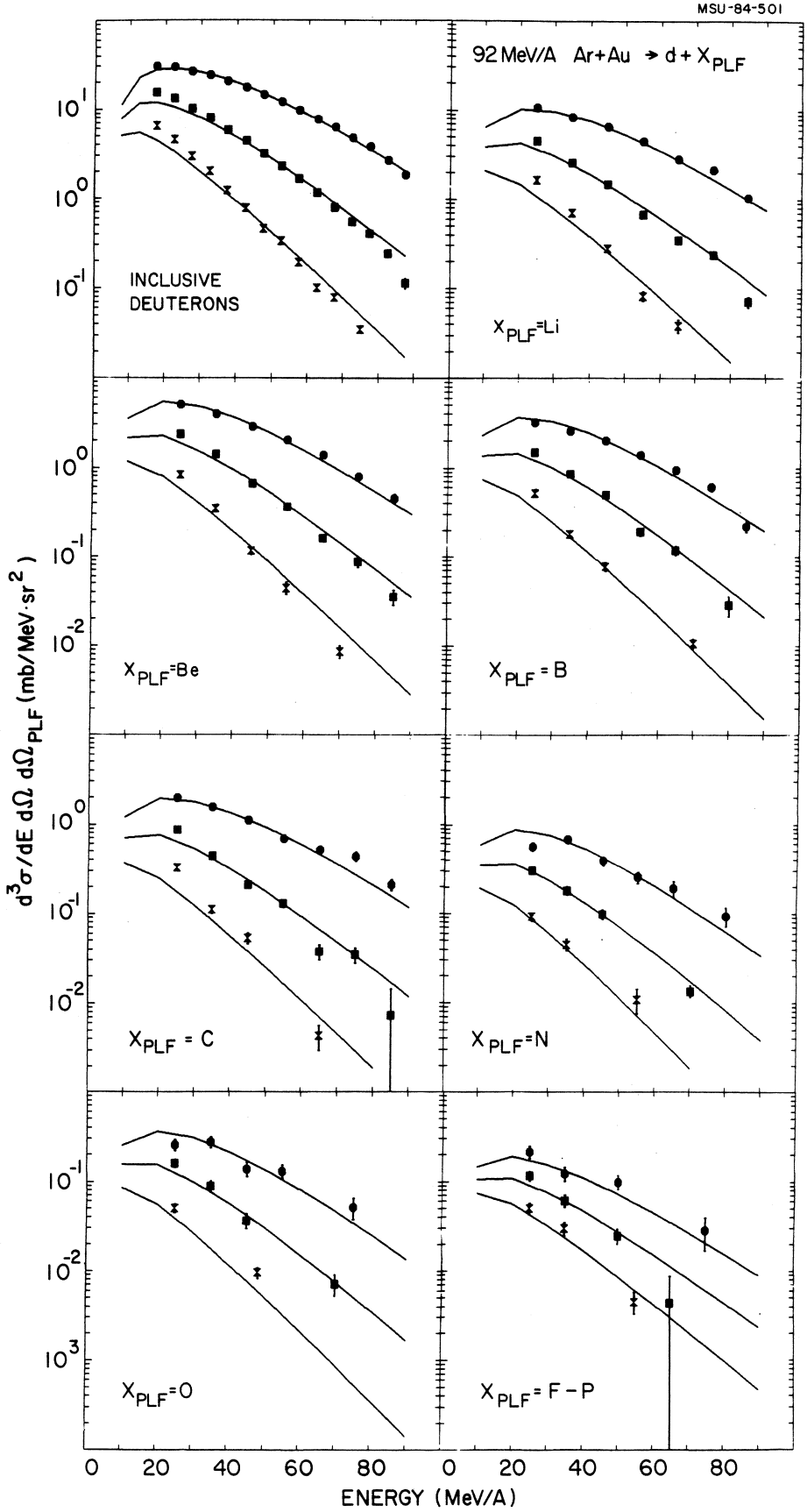
MSU-84-501
92 MeV/A Ar+Au → d + X_PLF
INCLUSIVE DEUTERONS
X_PLF=Li
X_PLF=Be
X_PLF = B
X_PLF = C
X_PLF=N
X_PLF=O
X_PLF= F - P
d³σ/dE dΩ dΩ_PLF (mb/MeV·sr²)
ENERGY (MeV/A)
0 20 40 60 80

Fig. 23

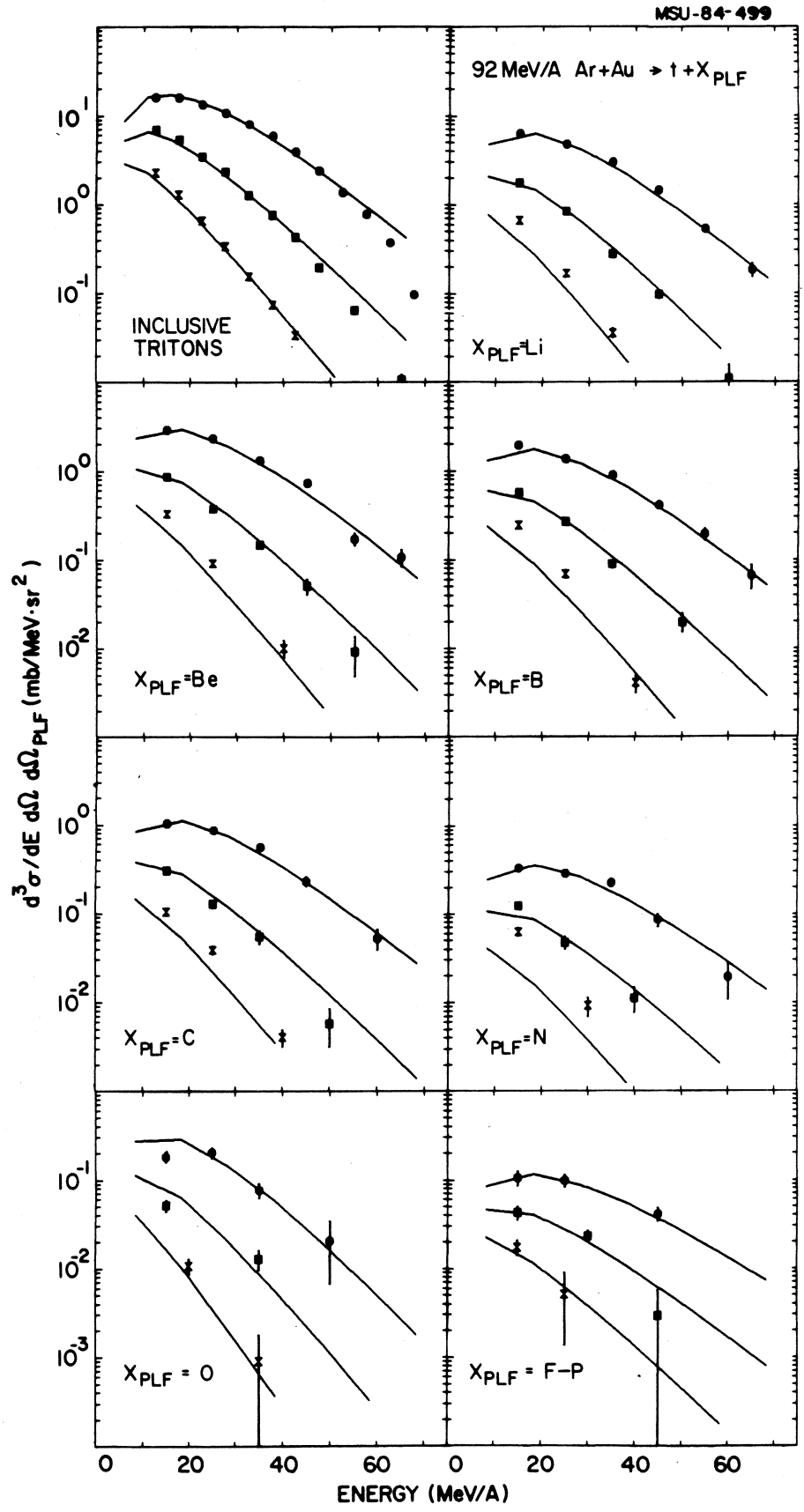
MSU-84-499
92 MeV/A Ar+Au → t + X_PLF
INCLUSIVE TRITONS
X_PLF=Li
X_PLF=Be
X_PLF=B
X_PLF=C
X_PLF=N
X_PLF = O
X_PLF = F-P
d³σ/dE dΩ dΩ_PLF (mb/MeV·sr²)
ENERGY (MeV/A)

Fig. 24

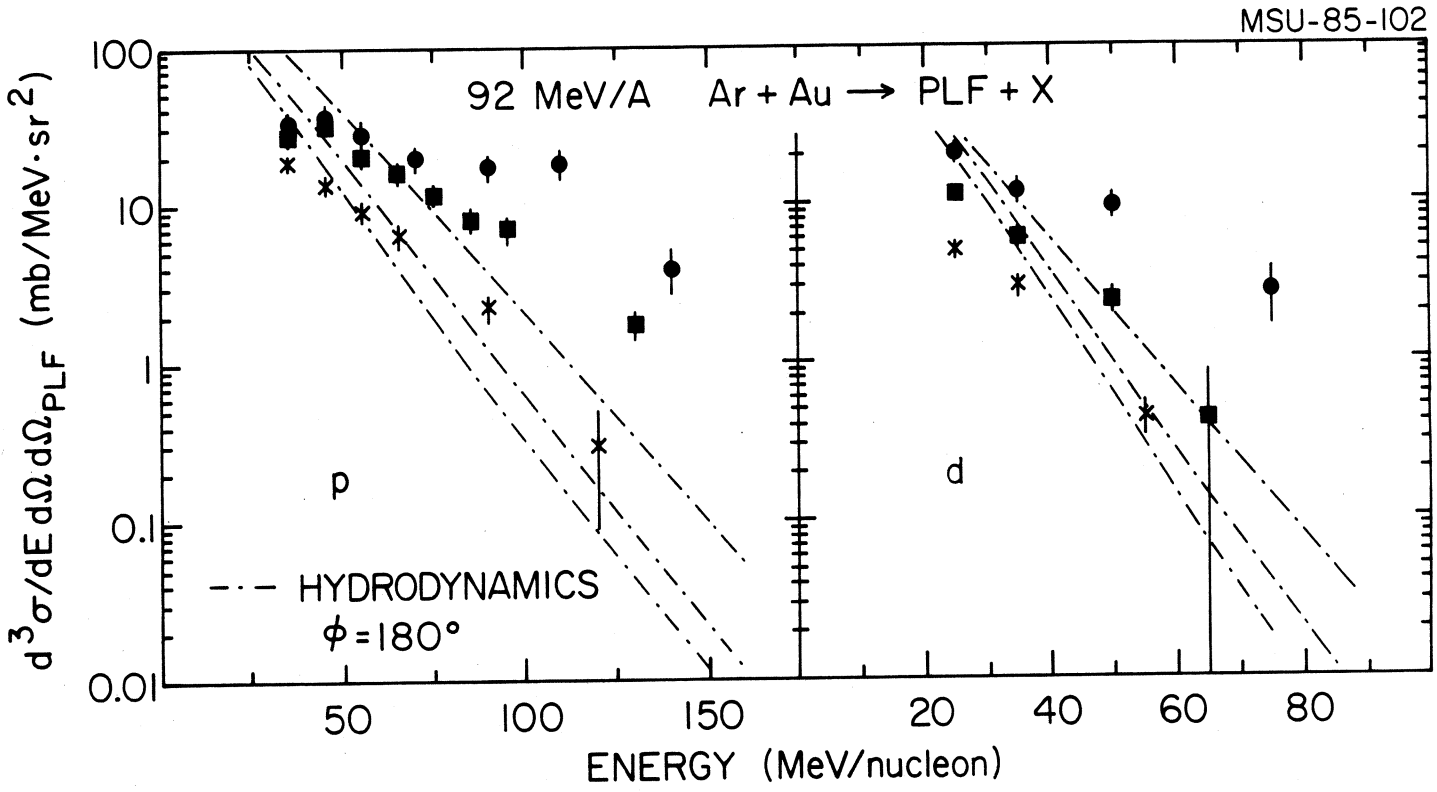
MSU-85-102
92 MeV/A Ar + Au → PLF + X
$d^3\sigma/dE\,d\Omega\,d\Omega_{PLF}$ (mb/MeV·sr^2)
100
10
1
0.1
0.01
p
d
HYDRODYNAMICS
ϕ=180°
50
100
150
20
40
60
80
ENERGY (MeV/nucleon)

Fig. 25